uOttawa

L'Université canadienne
Canada's university

FACULTÉ DES ÉTUDES SUPÉRIEURES ET POSTOCTORALES

u Ottawa

L'Université canadienne
Canada's university

FACULTY OF GRADUATE AND POSDOCTORAL STUDIES

Cole Van Vlack

AUTEUR DE LA THÈSE / AUTHOR OF THESIS

M.Sc. (Physics)

GRADE / DEGREE

Department of Physics

FACULTÉ, ÉCOLE, DÉPARTEMENT / FACULTY, SCHOOL, DEPARTMENT

Time Dependent Complex Scaling: Quantum Dynamics in Strongly Perturbed Systems

TITRE DE LA THÈSE / TITLE OF THESIS

Dr. T. Brabec

DIRECTEUR (DIRECTRICE) DE LA THÈSE / THESIS SUPERVISOR

CO-DIRECTEUR (CO-DIRECTRICE) DE LA THÈSE / THESIS CO-SUPERVISOR

EXAMINATEURS (EXAMINATRICES) DE LA THÈSE / THESIS EXAMINERS

Dr. L. Ramunno

Dr. R. Bhardwaj

Dr. J. Armitage

Gary W. Slater

Le Doyen de la Faculté des études supérieures et postdoctorales / Dean of the Faculty of Graduate and Postdoctoral Studies

MASTER'S THESIS

Time Dependent Complex Scaling: Quantum Dynamics in Strongly Perturbed Systems

Cole Van Vlack

Center for Photonics Research, University of Ottawa,

150 Louis Pasteur, Ottawa, ON, K1N 6N5 Canada

Thesis submitted to the Faculty of Graduate and Postdoctoral Studies and the Ottawa-Carleton Institute of Physics in partial fulfillment of the requirements for the MSc degree in Physics

Supervised by:

Thomas Brabec

Center for Photonics Research, University of Ottawa,

150 Louis Pasteur, Ottawa, ON, K1N 6N5 Canada

Your file Votre référence
ISBN: 978-0-494-50932-6
Our file Notre référence
ISBN: 978-0-494-50932-6

MASTER'S THESIS

Time Dependent Complex Scaling: Quantum Dynamics in Strongly Perturbed Systems

Cole Van Vlack

Center for Photonics Research, University of Ottawa, Ottawa, ON, K1N 6N5 Canada

E-mail: cvanv085@uottawa.ca

Abstract. We have begun development of a tool for investigating the bound state dynamics of single electron systems in intense fields. This was done by implementing the method of uniform complex scaling in a 1D test system in two different ways and have shown that the use of the "c-norm" in non-Hermitian quantum mechanics can fail for time dependent simulations. We have developed the method of complex backscaling which transforms the wavefunction from the complex scaled space back into real space and have shown that it is more robust than the "c-norm" and predicts the correct ionization when compared to simulations done in real space. We have also begun using the complex scaling method in a 2D N_2^+ model but it seems that the nature of the potential requires a more difficult type of scaling which causes problems within the calculations.

Contents

Acknowledgments

I would like to thank my wife Tasha for all her support and encouragement despite the fact that I am constantly biting off more than I can chew. Without your help I would never have been able to accomplish as much as I have.

I would also like to thank my supervisor Thomas Brabec for helping me to accomplish this thesis. Your patience has always been appreciated and I've really enjoyed the experience I've gained working with someone who has so much insight and knowledgeable about the field. I would also like to thank everyone else at the Centre for Photonics Reseach at the University of Ottawa, and in particular Charles Varin and Chris McDonald for the help and discussions you provided. As well, I would like to thank Thomas Fennel for helping me whenever I got stuck, and dedicating as much time as you did helping me with derivations. Finally, I would like to thank Mike Norris and Amelie Beausoleil for putting up with me here in Ottawa these last few months.

Chapter 1

Introduction

In many fields of physics, an extraordinary amount of work is done to determine the bound state dynamics of atoms and molecules in intense laser fields. Such processes are extraordinarily difficult to calculate but they also present many interesting effects that have yet to be understood. In atomic physics a good example is the non-sequential ionization [1][2] of an atom in an intense laser field (see Fig. 1.1). In this process we have an intense laser field ionizing the first electron and pulling it away from the nucleus. When the electric field changes sign, the ionized electron is accelerated back into the core where it interacts with the bound electron and causes it to be ionized. It is known that the mechanism for the first electron being ionized is tunnel ionization, but it is unclear the processes involved during the ionization of the second electron. Recent work has been done by C. McDonald using the multi-configuration time dependent Hartree-Fock method [3] to solve the fully coupled two electron system, but the two electron dynamics are so complicated that it is difficult to develop a model to understand the results. If we could examine the effects of the intense laser field, as well as the effects of the local electric field of the first electron, we may be able to follow the path by which the second electron is ionized.

Another example, related to attosecond science is the double ionization by an attosecond XUV laser pulse (see Fig 1.2) [4] [5] [6]. In such a process we use an attosecond pulse to ionize the first electron, this electron is immediately ejected from the core but it imparts enough energy

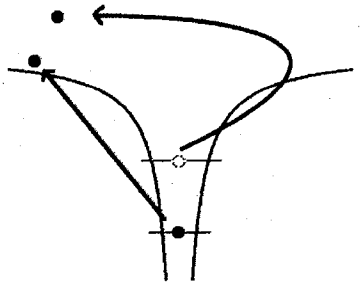

Figure 1.1. A schematic of non-sequential ionization where the first electron is pulled from the core by an intense laser field and then is accelerated back towards the core. When the first electron reaches the core again it interacts with the second bound electron and causes it to be ionized.

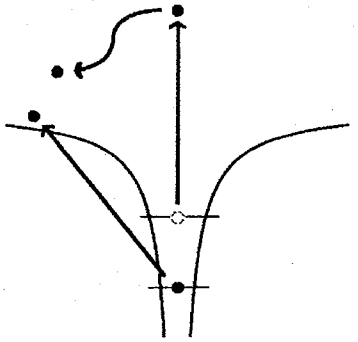

Figure 1.2. A schematic of attosecond XUV ionization. In this process the first electron is excited by the XUV pulse which shares it's energy with the second electron causing them both to become ionized

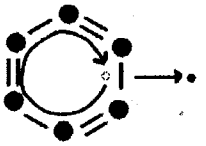

Figure 1.3. A schematic of a benzene ring that has been ionized and is left with an electron hole.

to the second bound electron that it is able to escape as well. An issue with such experiments is that high intensity attosecond pulses are extremely hard to obtain, so a probe in the form of an intense infra-red pulse is used to examine the dynamics. Such a probe has the effect of altering the electronic configuration of the core and it is unclear how this probe pulse distorts the dynamics of attosecond ionization.

A final example, coming from molecular physics, involves the ionization of benzene (see Fig. 1.3). When benzene is ionized a hole is left in the molecule which travels around the molecule in time. This hole can can drastically change the molecular dynamics of the system, especially when we have the ring attached to another molecule. In this case and in others the molecular dynamics are controlled by the resonances in the system, and such bond creations and destructions can happen on the attosecond timescale [7].

One characteristic that all of these effects have in common is that the intense, time dependent fields around the system change the dynamics of the system compared to the low intensity regime. The dynamics of these systems in intense fields is dominated by the fact that these intense fields create resonance states. A resonance state is a state whose energy lies within the continuum of the system but the state has a much longer lifetime than a traditional continuum state and displays bound state characteristics. These resonance states are formed by a density of states, where the energy width of the peak in the density of states is inversely proportional to the lifetime of the state. Resonances can be present in certain unperturbed systems, but they are more commonly created when an unperturbed system has a strong field incident on it which significantly alters the potential. When this happens states which were previously bound are suddenly in the continuum, but they retain some of their bound state properties. A schematic of such states is shown in Fig. 1.4.

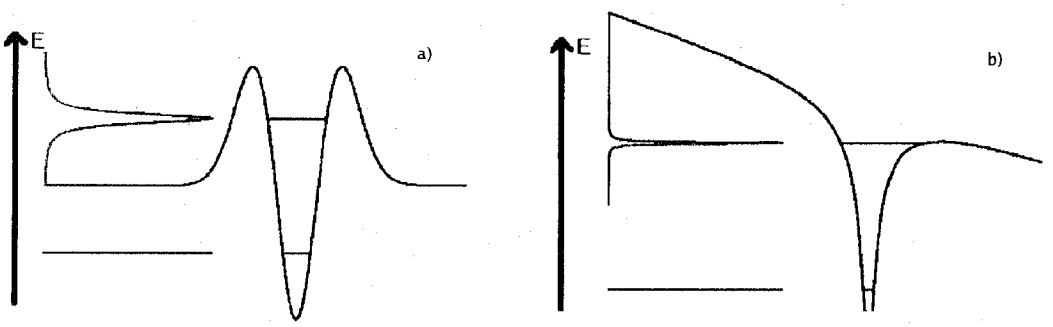

Figure 1.4. A schematic of a) A potential well with a potential barrier on either side. Such a potential has a bound state which has an energy less than zero and a resonance state whose energy is shown as a band of continuum states. b) An atomic potential with an applied electric field. The ground state of the system isn't significantly altered, but the energy of the first excited state is now located within the continuum and is made up of a band of continuum states

Complex scaling (also known as the complex coordinate method or the complex basis function method) is a method that has been used for many years in atomic, molecular and nuclear physics that allows a resonance state to be associated with a single, square-integrable, eigenfunction. The method essentially lifts the coordinates of the system into the complex plane and the dynamics are described by solving the Schrödinger equation with these complex coordinates. When this happens, the resonance state gains an imaginary part to its energy which is associated with the lifetime of the resonance state. States that were bound states before complex scaling continue to have a purely real energy after complex scaling which is consistant with the fact that bound states shouldn't decay. This method is very powerful as a way of imposing boundary conditions, as well as calculating the energies and lifetimes of a system. However, it becomes very difficult to obtain the true wavefunction of the system, and hence the probability of the wavefunction being within any of the eigenstates of the system. This is due to the fact that our Hamiltonian becomes a complex symmetric matrix (and hence non-Hermitian). The mathematics for complex symmetric matrices is shown in this thesis to lead to an unphysical norm. But, we shall develop the complex scaling method and propose a solution to the problem of the norm which plagues the method. We shall then implement our solution and show that time dependent dynamics can be calculated with our method.

In Chapter 2 we will describe the complex scaling method, and discuss it's origins, as well as derive a new complex scaled Hamiltonian that will allow us to calculate bound and resonance eigenstates. We will then talk about the difficulties in using these resonance eigenstates in calculating probabilities and propose a solution which will allow us to calculate such probabilities. In Chapter 3 we will develop two methods for propagating complex scaled eigenstates within an electric field, and extracting the path an electron takes as it ionizes. In Chapter 4 we will implement of all the above methods in a 1 dimensional test potential, and perform time dependent calculations which show that our method properly describes the time dependent dynamics. In Chapter 5 we will show how we have implemented complex scaling in a two-dimensional N_2^+

model and discuss issues relating to our implementation.

Chapter 2

Complex Scaling

When we look to solve for eigenfunctions of a system, it is implied that the states that we are looking for are the bound states of the system. But many systems form so called resonance states, which are states within the continuum that are significantly long lived. The use of resonance states can be instrumental to the explanation of many atomic and molecular processes, and prior knowledge of these states is extremely useful.

To illustrate how resonances form within system we start with a sample diatomic potential

$$V = -\frac{1}{\sqrt{(x-a)^2+s^2}} - \frac{1}{\sqrt{(x+a)^2+s^2}} \tag{2.1}$$

where $2a = 8.32$ a.u. is the separation between the nuclei and $s = 0.7129$ a.u. is a smoothing paramater. The parameters given are typical parameters of such a system. The eigenstates of this system can then be calculated using any number of methods, such as using a basis set and calculating the matrix elements or employing a space grid and solving the Hamiltonian along it (for methods of calculating eigenstates see appendix A). Fig. 2.1 shows the first 10 eigenstates of this sample potential calculated using the space grid method (see Sec. A.1). We can calculate many more than 10 states, such that the energy of the states becomes positive and the states are contained within the entire volume of the simulation range. These states correspond to continuum states and are "box-normalized". Normalizing regular continuum states involves delta function normalization in k space, but because of the finite width of the box, the eigenstates have a finite energy spacing (which also gives a finite k spacing) and must be normalized like bound states, hence the normalization depends on the box.

We can apply an electric field, F, to the above potential by adding an additional term of $-Fx$, and then blindly recalculate the eigenstates using the space grid method again. Fig. 2.2 shows the consequences of adding such a field. When we add the electric field, the point of lowest energy stops being within the potential well and the wall of the simulation volume and the bent potential form a new potential well. Because of this well, when eigenstates are calculated the eigenstates with the lowest energy stop being in the potential created by the diatomic molecule and start being in the pseudo well created by the potential and the wall of the simulation volume. The states caught in this pseudo well correspond to continuum states. Also, in the region where the excited states of the field free potential were located, the potential well has opened up which allows the previously bound states to become unbound and are then located within the continuum. When this happends we consider the states to be resonance states as they are characterized by the fact that they decay because they strongly couple to the continuum. This means that instead

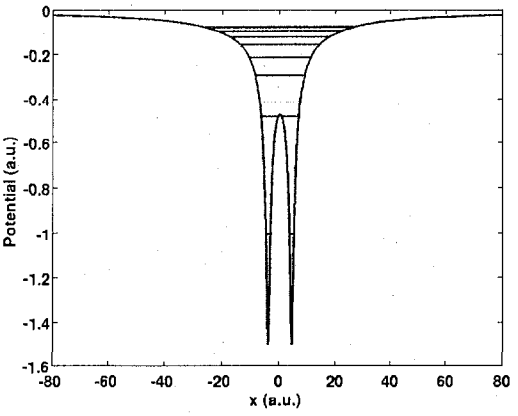

Figure 2.1. Example diatomic potential with first ten energy levels calculated with the space grid representation method with no external electric field present. The potential is given by Eq. 2.1

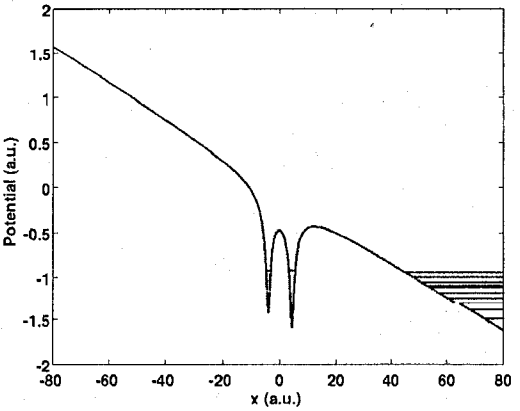

Figure 2.2. As Fig. 2.1 but with an external electric field of $F = 0.02$ a.u.

of having a discrete energy their discrete energy instead becomes a distribution of energies, also called a density of states. This is shown schematically in part b) of Fig. 1.4.

It may be possible to calculate the resonance energies in our case as well using our box normalized continuum states, but we must ensure we have a fine enough energy resolution to calculate a density of states. To get a finer resolution we must extend our simulation volume, but this creates more room for our eigenstates to "pool" along the side of the simulation range and means we must calculate more eigenstates again. This becomes quickly unfeasible and even after we have the energies, our resonance wave function consists of all of the eigenstates that contribute to the peak in the density of states, meaning that coupling from a bound state to a resonance state requires coupling to all of these states.

When implementing boundary conditions for a resonance state, because the resonance is

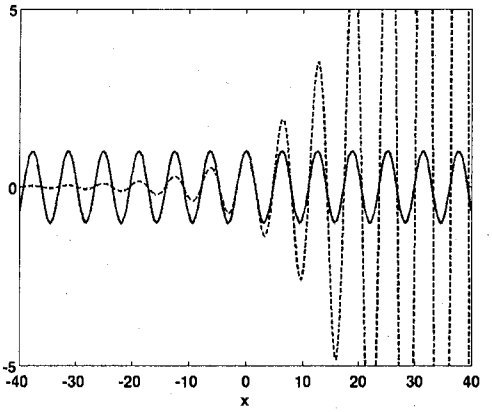

Figure 2.3. Plots of the real parts of e^{ikx} where the wavenumbers are $k = 1$ (in solid blue) and $k = 1 - i\delta$ (in dashed green) illustrating how outward traveling waves become divergent for Siegert states.

always decaying we must enforce that the flow of probability must always be outwards. This means that we must have outward boundary conditions or, as $x \rightarrow \infty$, the solution to our wavefunction is a plane wave, $\psi(x) \rightarrow e^{ikx}$, with wavevector k. Siegert was the first to implement such states [9] (so called Siegert states, Fig. 2.3), but the enforcement of this boundary condition leaves us with a non-Hermitian matrix, and gives the energies of such states an imaginary part, ie $E \rightarrow E + i\delta$. Since the kinetic energy and the wave vector are related by, $E \propto k^2$, this leaves k with a negative imaginary part, and causes such states to rapidly diverge with increasing x [10].

Complex scaling is a method that allows resonance states to be associated with a *single, square integrable* eigenfunction of a Hamiltonian that is analytically continued into the complex plane, as well as calculating bound states normally [8]. This continuation has the added benefits of enforcing the outgoing boundary condition, while simultaneously damping the divergence related to Siegert states, and adding an imaginary part to the energy which is directly related to the lifetime, Γ, of the eigenstate ($Im(E) = -\Gamma/2$ where Γ is real and $\Gamma \geq 0$). This damping of the Siegert states is due to the fact that we let our coordinates take on a complex value such that $\mathrm{Re}(ikz) < 0$ and instead of diverging, plane waves decay. This means that our resonances are taken from a density of states as in Fig. 1.4 with a linewidth to a single discrete state with a complex energy. The method was originally derived for use in scattering problems to circumvent the explicit enforcement of asymptotic boundary conditions, a good review of which was done by Reinhardt [10] and more recently by Moiseyev [8] who covers complex scaling in other contexts. The simplest picture of how complex scaling works is a description by Rescigno *et. al.* [11]. If we consider a single particle wave function in real space $\Psi(r)$ which undergoes a rotation of angle θ

$$\Psi(r) \Longrightarrow e^{i\theta/2}\Psi\left(e^{i\theta/2}r\right) \tag{2.2}$$

where $\theta \in R$, then this corresponds to a rotation through an angle θ and corresponds to a unitary transformation of the Hamiltonian from $\hat{H}$, to $\hat{H}_\theta = U(\theta)\hat{H}U^{-1}(\theta)$. Because we are performing a unitary transformation on the Hamiltonian then the spectrum of our Hamiltonian $\hat{H}_\theta$ is the same as $\hat{H}$ and eigenfunctions of $\hat{H}_\theta$ are simply rotated by an angle θ compared to the

eigenfunctions of $\hat{H}$.

In complex scaling we allow $\theta \in C$ and our transformation is no longer unitary. This rotates the continuum eigenvalues into the complex plane, and uncovers the resonances hidden by the first Riemann sheet (see Fig. 2.4). A proof of this is given by Simon [12] but is very involved and is beyond the scope of this thesis.

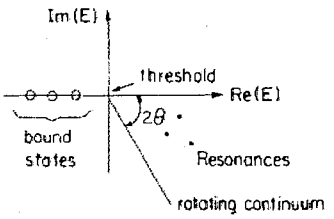

Figure 2.4. Schematic of complex scaled eigenvalues, showing bound states, the rotated continuum and the uncovered resonances. Figure taken from [8].

2.1 Complex Scaling

To derive our complex scaling equations we will start with a wavefunction already in a general complex space and derive it in terms of real space coordinates. There are plenty of papers which derive these transformations but ours will follow more closely those done by Karlsson [13]. This derivation is done for a general transformation, but we describe the transformations in Sec. 2.2, and show them in Fig. 2.5. If we consider a complex scaled coordinate z, and the 1D Schrödinger equation with a complex energy $E = \epsilon - i\Gamma/2$, where ϵ is the real part of the energy and is the same as the energy in the regular time independent Schrödinger equation, and $2/\Gamma$ is the lifetime of wavefunction. Then, the complex scaled wave function solves

$$\hat{H}_\theta \Psi(z) = E\Psi(z), \tag{2.3}$$

where the Hamiltonian (in a.u.) is

$$\hat{H}_\theta = -\frac{1}{2}\frac{d^2}{dz^2} + V(z). \tag{2.4}$$

We wish to represent this Hamiltonian terms of the real space coordinate x, so we must define a coordinate transformation,

$$z = Q(x), dz = q(x)\,dx \tag{2.5}$$

which will allow us to define a new wavefunction (in terms of the real coordinate)

$$\phi(x) \equiv \sqrt{q(x)}\Psi(Q(x)) \tag{2.6}$$

The simplest transformation that is used in complex scaling is just rotating the x axis into the complex plane with an angle θ (ie $z = xe^{i\theta}$). The new wavefunction $\phi(x)$ can then be

orthogonalized in real space coordinates without any scaling factors as they are included in the definition of $\phi(x)$. We can now start to rebuild the complex scaled Schrödinger equation. We start by deriving our derivative

$$\frac{d}{dx} = \frac{d}{dz}\frac{dz}{dx} \Longrightarrow \frac{d}{dz} = \frac{1}{q(x)}\frac{d}{dx} \tag{2.7}$$

$$\frac{d^2}{dz^2} = \frac{1}{q(x)}\frac{d}{dx}\frac{1}{q(x)}\frac{d}{dx} \tag{2.8}$$

Then applying 2.8 to our wavefunction $\phi(x)$ gives us (noting that the primes are derivatives with respect to x),

$$\begin{aligned}
-\frac{1}{2}\frac{1}{q}\frac{d}{dx}\frac{1}{q}\frac{d}{dx}\frac{1}{q^{1/2}}\phi &= -\frac{1}{2}\frac{1}{q}\frac{d}{dx}\frac{1}{q}\left[-\frac{1}{2}\frac{q'}{q^{3/2}}\phi + \frac{1}{q^{1/2}}\phi'\right] \\
&= -\frac{1}{2}\frac{1}{q}\frac{d}{dx}\left[-\frac{1}{2}\frac{q'}{q^{5/2}}\phi + \frac{1}{q^{3/2}}\phi'\right] \\
&= -\frac{1}{2}\frac{1}{q}\left[\frac{5}{4}\frac{q'^2}{q^{7/2}}\phi - \frac{1}{2}\frac{q''}{q^{5/2}}\phi - 2\frac{q'}{q^{5/2}}\phi' + \frac{1}{q^{3/2}}\phi''\right] \\
&= -\frac{1}{2}\frac{1}{q^{1/2}}\left[\left(\frac{5}{4}\frac{q'^2}{q^4} - \frac{1}{2}\frac{q''}{q^3}\right)\phi - 2\frac{q'}{q^3}\phi' + \frac{1}{q^2}\phi''\right]
\end{aligned} \tag{2.9}$$

Currently the ϕ' terms are the only terms within the second derivative that aren't symmetric, so to remove them lets calculate the symmetric term $\frac{1}{q}\frac{d^2}{dx^2}\frac{1}{q}\phi$.

$$\begin{aligned}
\frac{1}{q}\frac{d^2}{dx^2}\frac{1}{q}\phi &= \frac{1}{q}\frac{d}{dx}\left[-\frac{q'}{q^2}\phi + \frac{1}{q}\phi'\right] \\
&= \left[\frac{2q'^2}{q^4} - \frac{q''}{q^3}\right]\phi - \frac{2q'}{q^3}\phi' + \frac{1}{q^2}\phi''
\end{aligned} \tag{2.10}$$

Then equating 2.9 and 2.10 gives

$$\begin{aligned}
-\frac{1}{2}\frac{d^2}{dz^2} &= -\frac{1}{2}\frac{1}{q}\frac{d}{dx}\frac{1}{q}\frac{d}{dx}\frac{1}{q^{1/2}}\phi \\
&= -\frac{1}{2q^{1/2}}\left[\frac{1}{q}\frac{d^2}{dx^2}\frac{1}{q}\phi + \left(-\frac{3}{4}\frac{q'^2}{q^4} + \frac{1}{2}\frac{q''}{q^3}\right)\phi\right]
\end{aligned} \tag{2.11}$$

Finally, this leaves the equation 2.3, as

$$\begin{aligned}
\hat{H}_0\phi &= -\frac{1}{2}\left[\frac{1}{q}\frac{d^2}{dx^2}\frac{1}{q}\phi + \left(-\frac{3}{4}\frac{q'^2}{q^4} + \frac{1}{2}\frac{q''}{q^3}\right)\phi\right] + V(Q(x))\phi \\
&= E\phi
\end{aligned} \tag{2.12}$$

Extending this to 2D means we must just define our mapping from the complex coordinates (z_1, z_2) to the real space coordinates (x, y) by

$$\begin{aligned} z_1 &= Q(x), dz_1 = q(x)\,dx \\ z_2 &= P(y), dz_2 = q(y)\,dy \end{aligned} \tag{2.13}$$

Then, if we have $z_1 = x$ and $z_2 = y$ in some region, $\{x < x_0, y < y_0\}$, where the potential is non-zero and then complex scale in the region where our potential is zero, we may write our wavefunction as

$$\phi(x,y) = \sqrt{q(x)}\sqrt{p(y)}\Psi(Q(x), P(y)) \tag{2.14}$$

and our Schrödinger equation becomes

$$\begin{aligned} \hat{H}_\theta \phi(x,y) &= E\phi(x,y) \\ &= \begin{cases} \left[-\frac{1}{2}\frac{d^2}{dx^2} - \frac{1}{2}\frac{d^2}{dy^2}V(x,y)\right]\phi(x,y) & x < x_0, y < y_0 \\ -\frac{1}{2}\left(\frac{1}{q}\frac{d^2}{dx^2}\frac{1}{q} - \frac{3}{4}\frac{q'^2}{q^4} + \frac{1}{2}\frac{q''}{q^3}\right) - \frac{1}{2}\left(\frac{1}{p}\frac{d^2}{dy^2}\frac{1}{p} - \frac{3}{4}\frac{p'^2}{p^4} + \frac{1}{2}\frac{p''}{p^3}\right)\phi(x,y) & \text{else} \end{cases} \end{aligned} \tag{2.15}$$

Since we now have our complex scaled Schrödinger equation and wave function written in terms of our real coordinates, the only thing left to define is our general mappings, Eq. 2.5 and Eq. 2.13.

2.2 Complex Paths

Complex scaling, as originally proposed, had $q(x)$ defined as

$$q(x) = e^{i\theta} \tag{2.16}$$

This mapping, which we shall call from now on "uniform" complex scaling (UCS), was shown to work only for dilation analytic potentials, which essentially means potentials that don't contain any poles, and are spherically symmetric. For potentials that do contain poles, (ie have terms like $1/(z - z_i)$) "exterior" complex scaling was developed by Simon [14]

$$q(x) = \begin{cases} 1 & \text{if } |x| \le x_0 \\ e^{i\theta} & \text{if } |x| > x_0 \end{cases} \tag{2.17}$$

where complex scaling is "switched on" outside a finite hypersphere of radius x_0, which is generally at the point where the long range potential can be considered zero. This scaling causes problems with the derivative of the wavefunction as

$$\frac{dq}{dx} = \left(e^{i\theta} - 1\right)\delta(x - x_0) \tag{2.18}$$

where $\delta(x)$ is the Dirac delta function. This "sharp exterior" complex scaling (SHECS) lead to "smooth exterior" complex scaling (SMECS) which is defined by [11]

$$q(x) = \begin{cases} 1 & \text{if } |x| < x_0 - x_r \\ 1 + \left(e^{i\theta} - 1\right) g(x) & \text{if } x_0 - x_r \le |x| \le x_0 + x_r \\ e^{i\theta} & \text{if } |x| > x_0 + x_r \end{cases} \tag{2.19}$$

where $g(x)$ is a function that varies smoothly from 0 to 1, in the range $2x_r$ centered about x_0. For both (SHECS) and (SMECS), we can see immediately that we satisfy the conditions required to make the scaling given in Eq. 2.13.

Despite the limitations of UCS it is very desirable over SHECS and SMECS for a couple of reasons. The first is it's simplicity as all of the derivatives of q drop out of Eq. 2.12. The second reason is that, for zero electric field, the bound and resonance states are the only states that occupy the area around the potential well, and they are almost completely localized there. This means that when calculating the dipole moment, $\langle\phi_i|\, x\,|\phi_j\rangle$ between a continuum state, and either a bound or a resonance state, there is essentially no overlap. However, for SMECS our eigenvectors are always partially located near the potential well, because in the region around the potential well there is no scaling to separate the states into resonance and continuum. This is undesirable as the coupling between individual states goes as $\langle\phi_i|\, x\,|\phi_j\rangle / (E_j - E_i)$ (as explained further in Sec. 3.1.1), so if a continuum state becomes very close in energy to a resonance state there is an unphysical coupling due to the non-vanishing numerator.

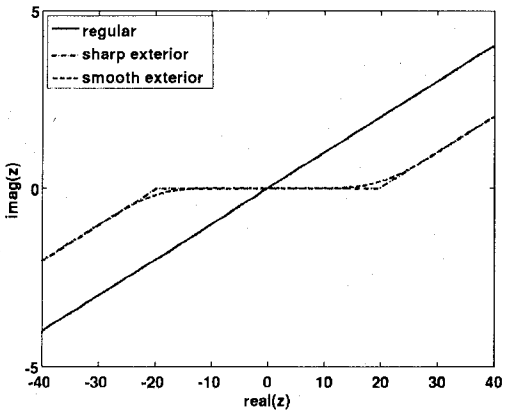

Figure 2.5. Here are examples of different complex scaling paths $z = Q(x)$ upon which the Schrödinger equation 2.3 is formulated. 1) The solid line is regular complex scaling with $\theta = 0.4$ (Eq. 2.16) 2) The dot-dashed line is SHECS with $\theta = 0.4$ and $x_0 = 20$ (Eq. 2.17) and 3) The dashed line is SMECS with $\theta = 0.4$, $x_0 = 20$ and $g(a) = \frac{1}{4}\left(2 + 3a - a^3\right)$ where $a = \frac{x - x_0}{x_r}$ 2.19. $g(a)$ was chosen in the same manner as Rescigno *et al* [11] as the lowest order polynomial that gives $g(-1) = 0$, $g(1) = 1$, $g'(-1) = 0$ and $g(1) = 0$ in order to ensure a smooth q and q' at $x = x_0 - x_r$ and $x = x_0 + x_r$

2.3 Complex Scaling and Inner Products

While complex scaling allows a nice analytical continuation of the Hamiltonian into the complex scaled domain, we are forced to deal with non-Hermitian quantum mechanics. The theory of inner products in a generalized space can be quite involved but Moiseyev [8] gives an argument for using a generalized inner product when using complex scaling and Gilary *et. al.* [15] show that this inner product give reasonable results when using complex scaling for a time independent

potential. When the method proposed by Gilary is used for a time dependent potential we find that the phases of the wavefunction lead to an unphysical picture of the norm.

When only applying the method of outgoing boundary conditions in the manner of Siegert [9] as mentioned above, our energies gain an imaginary part and are associated with a non-Hermitian Hamiltonian. Also, due to the rapid divergence of the eigenstates of this Hamiltonian the eigenstates are no longer part of a Hilbert space. Complex scaling also gives us a complex energy, but it simultaneously damps the wavefunctions at $x = \pm\infty$. This makes it much easier for performing calculations *within the complex scale space* but we need to be aware of how we can calculate a norm with physical meaning

Let us first consider a general matrix eigenvalue problem.

$$\hat{O}u_i = \lambda_i u_i \tag{2.20}$$

where, when the operator $\hat{O}$ operates on the right onto the eigenfunction u_i we obtain the eigenvalue λ_i. The adjoint eigenvalue equation, where the adjoint is defined by taking the conjugate transpose $\dagger = *T$, is

$$\hat{O}^\dagger v_i = \gamma_i v_i \tag{2.21}$$

where v_i is an eigenfunction of $\hat{O}^\dagger$ with eigenvalue γ_i. Now, when we make an inner product between any two functions a and b we perform the inner product as

$$\langle a|b\rangle = \int_{-\infty}^{\infty} a^* b \, dx \tag{2.22}$$

Then, for a very broad class of operators it can be shown that the eigenfunctions of the operator are orthogonal to the eigenfunctions of the adjoint operator

$$\begin{aligned} \langle v_i|u_j\rangle &= \int_{-\infty}^{\infty} v_i^* u_j dx \\ &= \delta_{ij} \end{aligned} \tag{2.23}$$

We shall now look at two special cases. The first is when our operator is Hermitian, ie $O^\dagger = O$, and the second when our operator is complex symmetric, ie $O^\dagger = O^*$. When our operator is Hermitian, the operator and the adjoint have the same eigenvectors, as

$$\begin{aligned} \hat{O}u_i &= \lambda_i u_i \\ &= \hat{O}^\dagger u_i \end{aligned} \tag{2.24}$$

thus, for Hermitian operators, we have $v = u$ and $\gamma = \lambda$, and our inner product becomes the Hermitian inner product,

$$\begin{aligned} \langle v_i|u_j\rangle &= \langle u_i|u_j\rangle \\ &= \int_{-\infty}^{\infty} u_i^* u_j dx \\ &= \delta_{ij} \end{aligned} \tag{2.25}$$

When our operator is complex symmetric, then our operator and its transpose satisfy the same eigenvalue equation

$$\begin{aligned} \hat{O}u_i &= \lambda_i u_i \\ &= \hat{O}^T u_i \end{aligned} \tag{2.26}$$

Then, by taking the complex conjugate of Eq. 2.26 we see that

$$\begin{aligned} \hat{O}^{T*}u_i^* &= \hat{O}^\dagger u_i^* \\ &= \hat{O}^\dagger v_i \end{aligned} \tag{2.27}$$

thus, for complex symmetric operators, we have $v = u^*$ and $\gamma = \lambda^*$, and our inner product becomes

$$\begin{aligned} \langle v_i|u_j\rangle &= \langle u_i^*|u_j\rangle \\ &= \int_{-\infty}^{\infty} u_i u_j dx \\ &= \delta_{ij} \end{aligned} \tag{2.28}$$

Thus, the proper inner product to perform when using complex symmetric matrices, called the "c-product" is

$$\begin{aligned} \langle u_i^*|u_j\rangle &= \int_{-\infty}^{\infty} u_i u_j dx \\ &\equiv (u_i|u_j) \end{aligned} \tag{2.29}$$

This has two very important implications.

(i) The only norm that we have that is associated with physical probability is the Hermitian norm, Eq. 2.25. There have been many papers written discussing the ineffectiveness of blindly using the Hermitian norm with non-Hermitian matrices to try and calculate probabilities (such as Gilary *et al* [15] and the references therein).

(ii) With a time dependent wavefunction, Φ, we may write it as a superposition of eigenstates, ϕ_i,

$$\Psi = \sum_i c_i \phi_i \exp\left(-iE_i\right) \tag{2.30}$$

Then, when we wish to calculate the norm of the wavefunction, we must calculate

$$\begin{aligned} |(\Psi|\Psi)| &= \left|\sum_i \sum_j c_i c_j \exp\left(-i\left(E_i + E_j\right)\right)(\phi_j|\phi_i)\right| \\ &= \left|\sum_i c_i^2 \exp\left(-i2E_i\right)\right| \end{aligned} \tag{2.31}$$

Where there is no absolute value around the individual coefficients. This means that trying to observe the norm when not in a single eigenstate can lead to phase effects that are unphysical in the sense that you can spontaneously lose and gain norm in your wavefunction despite the fact that the individual coefficients maintain the same amplitude during these times.

These combined effects mean that if we were able to find a way in which we could use the complex scaled eigenfunctions to describe a system, but still be able to use the Hermitian norm in a Hilbert space we would be able to assign physical meaning to our eigenstates.

2.4 Backscaling

So we are now caught between two problems: 1) if we don't complex scale we must calculate many eigenstates and then associate our resonances with a density of states. 2) if we do complex scale, we can calculate our states but have difficulty associating with them any "actual" electron dynamics as the norm we must use is unphysical. So, in order to gain both advantages while avoiding the difficulties we have to find a way to use complex scaling to obtain our eigenfunctions but still use the Hermitian norm. This will be done using a new method which we will call complex backscaling (CB). For CB, we will calculate our eigenfunctions in the complex scaled space using the global basis method (see appendix A). This means that we will use an analytical basis set with a finite number of basis functions, we will calculate the matrix elements of the Hamiltonian and then we will diagonalize it to find our eigenvalues. To get the, ijth, matrix element of our Hamiltonian H, we take our basis functions $\zeta_i(x)$ and calculate

$$\begin{aligned} H_{ij} &= \left(\zeta_i\right| \hat{H}\left(Q\left(x\right)\right) \left|\zeta_j\right) \\ &= \int \zeta_i\left(x\right) \hat{H}\left(Q\left(x\right)\right) \zeta_j\left(x\right) q\left(x\right) dx \end{aligned} \tag{2.32}$$

if, for example, we use UCS for our transformation in 2.32 we get

$$H_{ij} = e^{i\theta} \int \zeta_i\left(x\right) \hat{H}\left(xe^{i\theta}\right) \zeta_j\left(x\right) dx \tag{2.33}$$

It is then easy to see if we make the transformation $x \rightarrow xe^{-i\theta}$ because we know our basis analytically. Then Eq. 2.33 becomes

$$H_{ij} = \int \zeta_i\left(xe^{-i\theta}\right) \hat{H}\left(x\right) \zeta_j\left(xe^{-i\theta}\right) dx \tag{2.34}$$

Thus, if we diagonalize 2.34, we will still get our complex scaled eigenvalues and eigenfunctions. But since we know the analytical form of our basis, we can simultaneously calculate what these states correspond to in real space by undoing our scaling. If we expand our wavefunctions as a superposition of either the complex scaled eigenstates or the backscaled eigenstates we can represent our wavefunctions in complex scaled space and in real space. These backscaled states will correspond to Siegert states which, as mentioned above, aren't contained in a Hilbert space and aren't Hermitian. While there is no mathematical proof to suggest using these states we believe that just being in real space will allow us to calculate probabilities, and we will later justify this with numerical results. Thus if we ensure that our backscaled basis functions are normalized in Hermitian space with the regular Hermitian norm and enforce the same normalization factors within the complex scaled space, the norm obtained should be the norm which relates to physical processes. This solves the problems we had in the previous section of using an unphysical norm, by letting us use the Hermitian norm that corresponds to probabilities in the real world and eliminates the unphysical interferences that we obtain with the "c-norm".

This method is the first method ever proposed to calculate such time dependent probabilities, as any of the literature thus far uses the "c-norm" for calculations. Once we have these backscaled states we plan on performing time dependent calculations in the complex scaled space, and then extracting information from them using our backscaled wavefunctions. This is illustrated in figure 2.6.

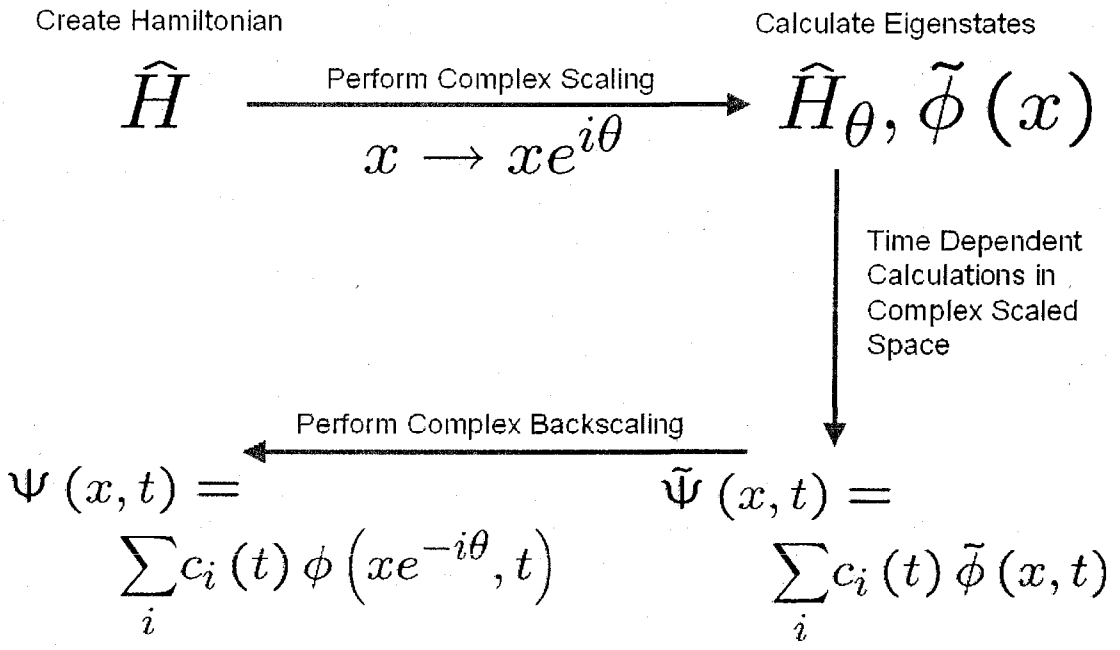

Figure 2.6. A Schematic of our plan for performing time dependent calculations using complex scaling. We first start with a Hamiltonian, and then apply complex scaling to calculate the field dependent eigenfunctions. We then perform time dependent calculations in the complex scaled space with these complex eigenfunctions as our basis and then backscale to get our wavefunction in real space.

Chapter 3

Time dependent model

Since we are able to calculate time independent field dressed eigenstates using complex scaling, it would be incredibly useful to be able to use such states in time dependent simulations. Previous calculations for time dependent simulations have been done by Plummer and McCann where they calculated the ionization rates of molecular hydrogen to perform calculations [16] and then applied complex scaling with Floquet theory to again obtain ionization rates [17]. Gilary *et. al.* also performed time dependent simulations using complex scaling to examine the effect of the generalized inner product on the dynamics of the system [15]. To allow a better understanding of the dynamics in complex scaled systems, we will develop a multilevel equation method with a field dependent, complex scaled dipole moment which will describe how the field dressed states react to the time dependent field. This multi-level method will then be compared to a method which directly propagates the wavefunction, in the complex scaled space and then in real space to check the agreement between the Multi-level equations .

3.1 Multi-level equations

Given a static field F, we can find the time dependent complex scaled eigenstates $\psi_i(F,\vec{x},t) = \phi_i(F,\vec{x})\, e^{-iE_i(F)t}$ which are solutions of the time dependent complex scaled Schrödinger equation

$$i\partial_t \psi_i(t,\vec{x}) = \hat{H}_0 \psi_i(t,\vec{x}) - FQ(x)\,\psi_i(t,\vec{x}) \tag{3.1}$$

where our energies E_i are complex. The time independent states, $\phi_i(F,\vec{x})$ are then solutions of

$$E_i(F)\,\phi_i(F) = \hat{H}_0 \phi_i(F) - FQ(x)\,\phi_i(F) \tag{3.2}$$

We then make the ansatz that our wavefunction can be written in terms of the eigenstates, $\phi_i(F(t),\vec{x})$, where we allow the electric field to be time dependent. We then rewrite our wavefunction as a superposition of these eigenstates and assume that they have a rotating phase term that depends only on the real part of the energy $\epsilon_i = Re(E_i(F(t)))$.

$$\Psi(t,\vec{x}) = \sum_i c_i(t)\,\phi_i(F(t),\vec{x})\, e^{-i\int_{t_0}^{t}\epsilon_i(F(t'))dt'} \tag{3.3}$$

because we have introduced time dependence back into our Hamiltonian by allowing F to be time dependent, we must resolve the time dependent Schrödinger equation, Eq. 3.1, by plugging

into it our ansatz, Eq. 3.3. This leads to

$$i\sum_i c_i(t)\,\partial_t\left(\phi_i(F(t),\vec{x})\right)e^{-i\int_{t_0}^{t}\epsilon_i(F(t'))dt'}+i\sum_i \partial_t\left(c_i(t)\right)\phi_i(F(t),\vec{x})\,e^{-i\int_{t_0}^{t}\epsilon_i(F(t'))dt'}+$$
$$\sum_i \epsilon_i c_i(t)\,\phi_i(F(t),\vec{x})\,e^{-i\int_{t_0}^{t}\epsilon_i(F(t'))dt'}$$
$$=\sum_i\left(\hat{H}_0-Fx\right)c_i(t)\,\phi_i(F(t),\vec{x})\,e^{-i\int_{t_0}^{t}\epsilon_i(F(t'))dt'} \quad (3.4)$$

which, when written in terms of the full energy becomes

$$i\sum_i c_i(t)\,\partial_t\left(\phi_i(F(t),\vec{x})\right)e^{-i\int_{t_0}^{t}\epsilon_i(F(t'))dt'}+i\sum_i \partial_t\left(c_i(t)\right)\phi_i(F(t),\vec{x})\,e^{-i\int_{t_0}^{t}\epsilon_i(F(t'))dt'}+$$
$$\sum_i E_i c_i(t)\,\phi_i(F(t),\vec{x})\,e^{-i\int_{t_0}^{t}\epsilon_i(F(t'))dt'}+i\sum_i\frac{\Gamma_i}{2}c_i(t)\,\phi_i(F(t),\vec{x})\,e^{-i\int_{t_0}^{t}\epsilon_i(F(t'))dt'}$$
$$=\sum_i\left(\hat{H}_0-Fx\right)c_i(t)\,\phi_i(F(t),\vec{x})\,e^{-i\int_{t_0}^{t}\epsilon_i(F(t'))dt'} \quad (3.5)$$

Then, we assume that the time dependent eigenstates $\phi_i(F(t),\vec{x})$ solve the time independent Schrödinger equation, Eq. 3.3, ignoring the dependence of the field on time

$$i\sum_i c_i(t)\,\partial_t\left(\phi_i(F(t),\vec{x})\right)e^{-i\int_{t_0}^{t}\epsilon_i(F(t'))dt'}+i\sum_i \partial_t\left(c_i(t)\right)\phi_i(F(t),\vec{x})\,e^{-i\int_{t_0}^{t}\epsilon_i(F(t'))dt'}$$
$$=-i\sum_i\frac{\Gamma_i}{2}c_i(t)\,\phi_i(F(t),\vec{x})\,e^{-i\int_{t_0}^{t}\epsilon_i(F(t'))dt'} \quad (3.6)$$

then using the orthogonality of the eigenfunctions $(\phi_j|\phi_i)=\delta_{i,j}$, and projecting with ϕ_j gives us a set of coupled differential equations for the coefficients

$$\partial_t c_j(t)=-\sum_i c_i(t)\,(\phi_j|\partial_t\phi_i)\,e^{-i\int_{t_0}^{t}\left(\epsilon_i(F(t'))-\epsilon_j(F(t'))\right)dt'}-\frac{\Gamma_j}{2}c_j(t) \quad (3.7)$$

applying the chain rule on $\partial_t\phi_i$ gives

$$\partial_t\phi_i=\frac{\partial\phi_i(F,\vec{x})}{\partial F}\frac{dF}{dt} \quad (3.8)$$

projecting with ϕ_j gives

$$(\phi_j|\partial_t\phi_i)=K_{ji}(F(t))\frac{dF}{dt} \quad (3.9)$$

where we define

$$K_{ji}(F(t))=\left(\phi_j|\frac{\partial\phi_i}{\partial F}\right) \quad (3.10)$$

Substituting Eqs. 3.8 - 3.10 into equation 3.7 leads to

$$c_j(t) = \int_{t_0}^{t} \sum_i c_i(t') K_{ji}(F(t')) \frac{dF(t')}{dt} e^{-i\int_{t_0}^{t'}(\epsilon_i(F(t'')) - \epsilon_j \Sigma_i(F(t')))dt''} - \int_{t_0}^{t} \frac{\Gamma_j}{2} c_j(t) \quad (3.11)$$

Thus, we can then find the time dependent c's for any time dependent electric field, as long as we have the field dependent eigenfunctions and energies.

3.1.1 Calculating the K coefficients

If we consider the time dependent Schrödinger equation with an unperturbed Hamiltonian H_0 and a time independent electric field, F

$$E(F)\Psi(F) = \hat{H}_0\Psi(F) - Fx\Psi(F) \quad (3.12)$$

that has eigenfunctions $\psi_i(F)$ and $E_i(F)$ and then apply a perturbation ΔF to the field we obtain

$$E_i(F+\Delta F)\psi_i(F+\Delta F) = \hat{H}_0\psi_i(F+\Delta F) - Fx\psi_i(F+\Delta F) - \Delta Fx\psi_i(F+\Delta F) \quad (3.13)$$

Using perturbation theory, we can calculate the perturbed wave function by

$$\psi_j(F+\Delta F) = \psi_j(F) + \sum_{j\neq i} c_i(F+\Delta F)\psi_i(F) \quad (3.14)$$

where, according to perturbation theory, we have for the c_i's

$$c_i(F+\Delta F) = -\Delta F \frac{(\psi_i(F)|x|\psi_j(F))}{E_j(F) - E_i(F)} \quad (3.15)$$

which allows us to write our full wave function at $F+\Delta F$ as

$$\psi_j(F+\Delta F) = \psi_j(F) - \Delta F \sum_{j\neq i} \frac{(\psi_i(F))x(\psi_j(F))}{E_j(F) - E_i(F)}\psi_i(F) \quad (3.16)$$

Then, using the definition of a derivative, we have

$$\begin{aligned} \partial_F\psi_j(F) &= \frac{\psi_j(F+\Delta F) - \psi_j(F)}{\Delta F} \\ &= -\sum_{j\neq i} \frac{(\psi_j(F)|x|\psi_i(F))}{E_i(F) - E_j(F)}\psi_i(F) \end{aligned} \quad (3.17)$$

Then, if we project with $\psi_i(F)$

$$\begin{aligned} (\psi_i(F)|\partial_F\psi_j(F)) &= -\frac{(\psi_j(F)|x|\psi_i(F))}{E_i(F) - E_j(F)} \\ &= K_{ij}(F) \end{aligned} \quad (3.18)$$

where we note that due to the $i \neq j$ in the summation $K_{ii} = 0$. Because we are using the "c-norm" there seems to be some ambiguity as to what energy, E_i should be used but testing showed that using the full energy, $E_i = \epsilon_i - \Gamma_i/2$ was not appropriate and just using the real parts of the energy gave the best agreement.

3.2 Explicit time dependent propagation

In order to check our multilevel equations a separate method of time propagation is needed. Since we are already calculating Hamiltonians in order to calculate eigenfunctions, the simplest way of propagating our wavefunction is by using the Schrödinger equation explicitly.

$$\begin{aligned}\psi(\Delta t) &= \psi(0) + \Delta t \left.\frac{d\psi}{dt}\right|_0 \\ &= \psi(0) - \frac{i\Delta t}{\hbar}\hat{H}(0)\psi(0) \\ &= \left[1 - \frac{i\Delta t}{\hbar}\hat{H}(0)\right]\psi(0) \\ &\simeq \exp\left[-\frac{i\Delta t}{\hbar}\hat{H}(0)\right]\psi(0)\end{aligned} \tag{3.19}$$

For a time dependent Hamiltonian this leads to

$$\psi(t) = \prod_{n=0} \exp\left[-\frac{i\Delta t}{\hbar}\hat{H}(n\Delta t)\right]\psi(0) \tag{3.20}$$

It is then possible to project onto the time dependent wave-function using the field dependent eigenfunctions since we know the time dependence of the field. This allows us to calculate our c_i coefficients in two different ways for a direct comparison.

Chapter 4

One dimensional test model

The code we wrote to perform our complex scaling calculations was done entirely in Matlab. The decision to use Matlab was motivated by a couple of factors: 1) we needed an eigensolver, and Matlab had already implemented the eigensolver LAPACK 2) we had originally implemented complex scaling in 2D to connect to other simulations done using N_2 which meant memory was an issue. When we first implemented the space grid representation for a grid of n_x by n_y points, you would have to have Hamiltonian that is $n_x n_y \times n_x n_y$. For 200 points per side we would have 1.6e9 elements and for 16 byte complex numbers we would need 25.6 GB of memory, which is completely unreasonable on a single machine. ARPACK, which is an eigensolver that was considered employs a banded style format that assumes that most of the elements not contained within a "band" of elements centered around the diagonal are zero, but this gave a Hamiltonian which had approximately $4n_x n_y^2$ or 3.2e7 elements (512 MB of memory) but this still seemed prohibitive.

Matlab allows the use and diagonalization of sparse matrices which are matrices where all elements are treated as zero unless they are specifically allocated. In 2D, if we were to use the derivative proposed in appendix A, we would need $n_x n_y$ points for the diagonal and approximately $8n_x n_y$ points for each derivative leading to only 3.6e5 points and 5.76 MB of memory. This is a huge gain in terms of memory compared to allocating the entire matrix (~4e4) or using the ARPACK solver (~80), and suddenly the problem is not only feasible, but easily implemented. We are testing our method in 1D so we have the luxury of using many more points than we have in 2D, but we have performed some calculations in 2D using N_2 as our potential. Even so it is worth knowing that 2D simulations and even 3D simulations have a possibility (for 3D 1.7 GB for a box of 200 points per side).

4.1 Time Independent Calculations

4.1.1 Space Grid method

For our testing we have started with a potential very similar to the potential used by Gilary *et. al.* [15], where the only change is in the height of the bounding part of the potential. This was done so that we obtained only 2 states, a single bound state and a resonance state. The potential, in a.u., is

$$V(x) = -\frac{1}{2}\frac{d^2}{dx^2} = \left(\frac{x^2}{2} - 0.8\right)\exp(-0.19x^2) \tag{4.1}$$

For our complex scaling, we implemented uniform complex scaling which means that all of the derivative terms in Eq. 2.12 drop out to give us

$$E\phi(x) = -\frac{1}{2}e^{-2i\theta}\frac{d^2}{dx^2}\phi(x) + V(Q(x))\phi(x) \tag{4.2}$$

When we performed simulations using the space grid method we ended up using $n_x = 5401$ points along a range of ± 80 to give an x spacing of $\Delta x = 0.0296$. Such high spatial resolution was required to properly calculate the continuum-like eigenstates which oscillate quite rapidly. The scaling angle which was found to give the best scaling results, as well as being the best scaling angle for the global basis function method was $\theta = 0.1$. For a description of how the Hamiltonian was calculated please see Appendix A.

The eigenstates were calculated for electric field values from $F = 0$ to $F = 0.02$ in steps of $\Delta F = 0.0001$, and for each field value 150 eigenstates were calculated. The resonances were identified in the $F = 0$ case by examining graphs of the real and imaginary parts of the energies (Fig. 4.1), where the bound states are easily identifiable as having $Re(E) < 0$ and the resonances are identifiable as being separate from the rotated continuum states. There appears to be a splitting of the continuum states in the center of the rotated continuum, but we believe that these states were degenerate states before complex scaling (ie plane waves with wavevector $\pm k$). After complex scaling the degeneracy seems to have lifted and the energies of these states becomes separated.

The eigenstates are ordered according to energy, but as the electric field tilts the potential the continuum states are constantly moving lower in the spectrum. This means, if the resonance is in state $i = 10$ in the $F = 0$ eigenstate calculation, the resonance is not necessarily at $i = 10$ in the $F = \Delta F$ eigenstate calculation. In order to properly track our ground and resonance states for use in the time dependent calculations, the overlap between the ground and resonance states ,$\phi_{g/r}(F_0)$, at $F = F_0$ and all other eigenstates, $\phi_i(F_0 + \Delta F)$, for $F = F_0 + \Delta F$ was calculated, $\left(\phi_i(F_0 + \Delta F)|\phi_{g/r}(F_0)\right)$. The resonance and ground states at $F = F_0 + \Delta F$ were then the states that had the largest overlap integral. Tracking such states is necessary if we are going to perform time dependent calculations involving the ground and resonance states as we want to make sure we are always using the correct state to describe the dynamics.

Since we can follow our states through the field, we are able to find the energy of the bound and resonance states as a function of the electric field (Figs. 4.2 and 4.3), and observe what these states look like in the complex scaled domain (Fig. 4.4). Although this has been done previously, it is worth pointing out how difficult this is without complex scaling. Calculating the field free resonance may be possible with a lot of work, but being able to calculate the resonance with an electric field and beyond the perturbative regime is unheard of without these methods. We must be careful with these eigenstates though, as they have only been calculated in the complex scaled space so we are not (yet) allowed to relate them to a physical wavefunction until we find a way of transforming them back into real space.

Some interesting points were discovered when we performed these calculations. The first is that the resonance state is continually mixing with continuum states and creating avoided crossings, but the signature of the resonance follows along a line which is level with the field free resonance energy. This can be seen in Fig. 4.2; as all of the continuum states that mix with the resonance come in from below they stay at the same energy as the resonance before moving higher into the continuum and mixing with the next continuum state. Thus, in order to follow our resonance for electric fields higher than 0.005 a.u., we must track more than two states in order to observe the full dynamics. These other states were found by looking at the eigenfunctions after the avoided crossing, and calculating the overlap backwards in terms of the

electric field to find the eigenstate at zero electric field which will evolve into the resonance. For electric fields up to 0.025 a.u. we required 17 eigenstates to cover all the bound and resonant states.

The second interesting feature is that as the potential tilts with the electric field, a second well is created between the "left arm" (See Fig. 4.4 particularly parts 2c) and 3c)) of the tilted field and the potential barrier. This surprising feature had the consequences of increasing the lifetime of the resonance as the electric field increased (Fig. 4.3 around $F = 0.005$ a.u.) and making the resonance more bound as the field increased. The complex scaled continuum states also behave in the same manner, coming in from states which quickly decay where they then get "trapped" in the pocket. It is a little counterintuitive that by adding an electric field, a resonance could become more bound, but this effect is borne out in the time dependent calculations.

4.1.2 Global Basis Function method

For complex scaled calculations using the global basis function method, we used Hermite Gaussians for our basis functions which look like

$$\zeta_n(x) = \left(\frac{1}{n!2^n w\sqrt{\pi}}\right)^{1/2} e^{-\frac{x^2}{2w^2}} H_n\left(\frac{x}{w}\right) \tag{4.3}$$

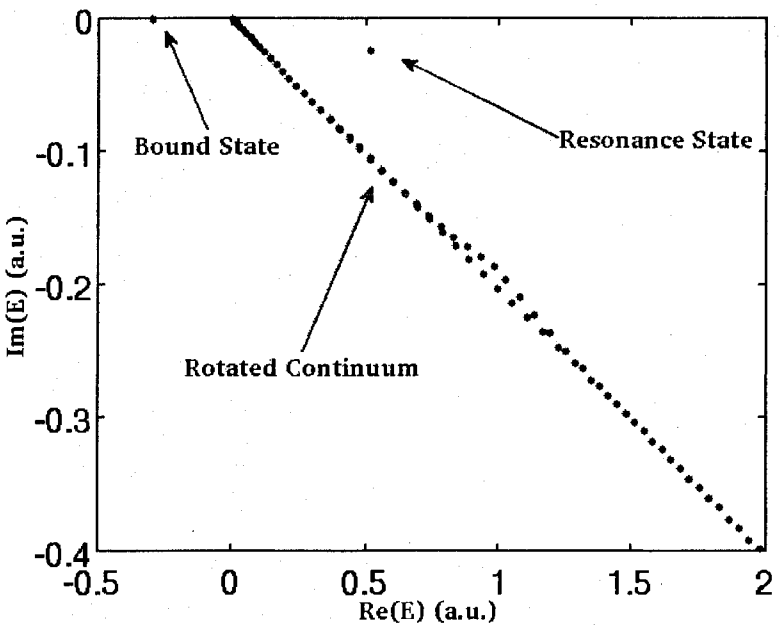

Figure 4.1. A plot of the real versus imaginary parts of the energy for the potential given in Eq. 4.1 with no electric field and a scaling factor of $\theta = 0.1$. The bound state is the state with Re(E) < 0, and the resonance is the state that is separated from the rotated continuum states.

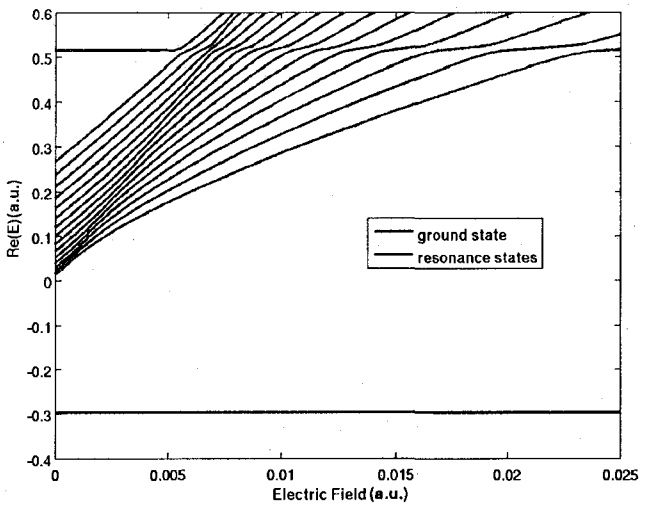

Figure 4.2. A plot of the real part of the energy of the ground state (in blue), and all of the states that couple to the resonance (in red). Between $F = 0$ a.u. and $F = 0.005$ a.u. our resonance state is the same state as shown in Fig. 4.1.

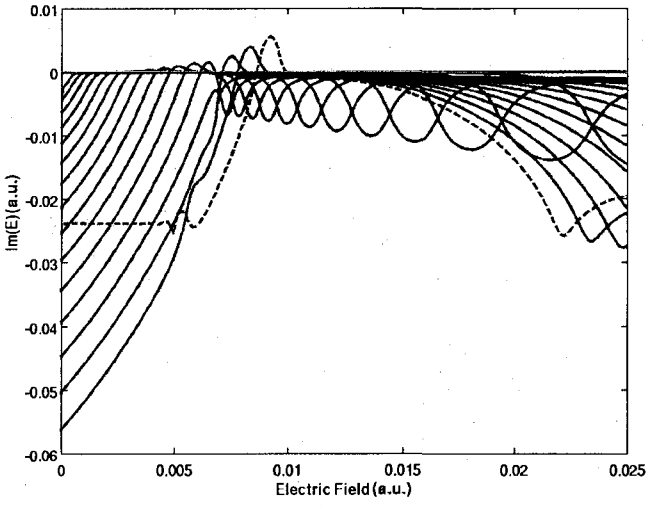

Figure 4.3. A plot of the imaginary part of the energy of the ground state (in blue), the state that is the resonance at $F = 0$ a.u. (in dashed red), and all of the states that couple to the resonance (in red).

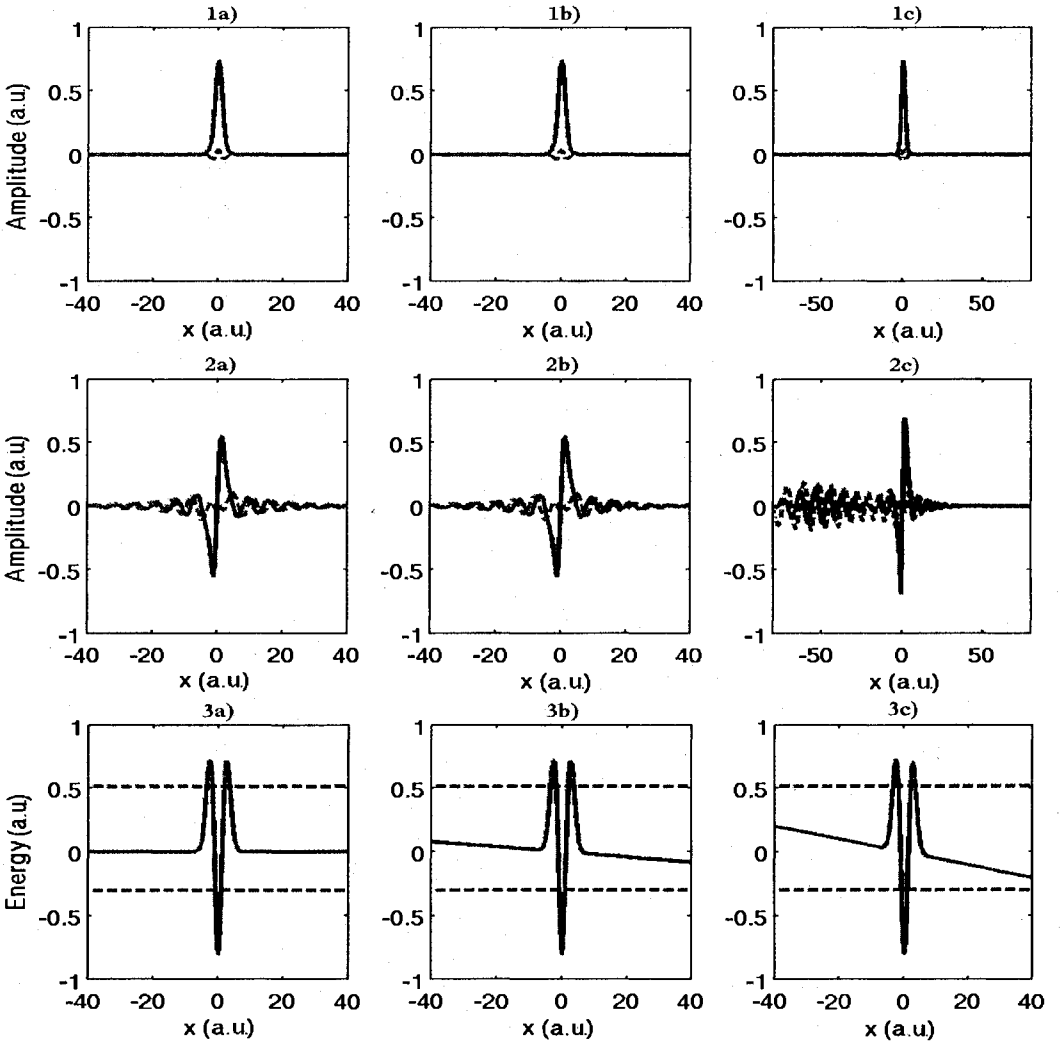

Figure 4.4. Plots of the real (solid line) and imaginary (dashed line) parts of 1) The ground state wavefunction for electric fields of a) $F = 0$ a.u. b) $F = 0.002$ a.u. and c) $F = 0.005$ a.u. 2) The resonance wavefunction for electric fields of a) $F = 0$ a.u. b) $F = 0.002$ a.u. and c) $F = 0.005$ a.u.. 3) A plot of the potential given in Eq. 4.1 with an applied electric field of a) $F = 0$ a.u. b) $F = 0.002$ a.u. and c) $F = 0.005$ a.u.. The real part of the energies of the ground state and the resonance state are given at each of these values (dashed red lines)

where $H_n(r)$, are the Hermite polynomials and w is a measure of the width of the basis functions. We used $\theta = 0.1$ as in the SGR, but convergence was much more difficult, especially if we try to ensure that our backscaled wavefunctions are converged (more on this in Sec 4.1.3). It turns out that any given potential requires a basis specifically tuned to that problem and a lot of work must be done to find a basis that gives good results. By using the SGR calculations as a comparison (ie calculating the overlap between the SGR eigenfunctions and the global basis eigenfunctions), many combinations of width parameters were chosen until eventually it seemed that using two basis sets of Hermite Gaussians gave the best convergence, especially if the widths of the two basis sets were far apart. The first set that was chosen had 50 functions with a width $w_1 = 1$ and the second had 20 functions with a width of $w_2 = 5$. Since the two basis sets were not orthogonal we needed to solve the generalized eigenvalue problem Eq. A.27, which required calculating the complex scaled space orthogonality matrix, O^{cs}, where the matrix elements are defined by $O^{cs}_{ij} = (\zeta_i(x)|\zeta_j(x))$.The calculations of the eigenstates and the orthogonality matrix is fully described in Appendix A. The ground, first excited state and an example continuum state for $F = 0$ a.u. are shown in Fig. 4.5.

4.1.3 Backscaling the Global Basis Functions

When we calculate our complex scaled wavefunctions, we are not in real space and must worry about the significance of the norm of our wave function. Initial time dependent calculations showed that our using the "c-norm" as a measure of the wavefunction is formally correct, but is misleading because the rotating phase terms are present in both $\psi(t)$, and $\psi(t)^2$, whereas in Hermitian quantum mechanics we wouldn't explicitly observe such effects because we use $|\psi(t)|^2$ as a measure of our norm. This will be shown in Sec. 4.2. To observe the "true" norm of our wavefunctions we need to bring them back into real space and then enforce the regular Hermitian norm.

Since we know the analytical form of our basis functions, we are able to calculate them in both the complex scaled space $\zeta_i(x)$ and backscaled to real space $\zeta_i\left(xe^{-i\theta}\right)$. When we recreate our eigenfunctions, we can then recreate them in complex scaled space (cs)

$$\phi^{cs}_m = \sum_i c_{mi}\zeta_i(x) \tag{4.4}$$

or in real space (rs) as described in Sec. 2.4

$$\phi^{rs}_m = \sum_i c_{mi}\zeta_i\left(xe^{-i\theta}\right) \tag{4.5}$$

Fig. 4.5 shows the effects of backscaling when we blindly normalize our wavefunctions in complex scaled space and then backscale. The amplitude of the resonance and the ground state remain reasonable (for the field free case) but we can see that the continuum state begins to rapidly diverge. This divergence would continue farther in x off to infinity, but the place where the wavefunction dies off again is the extent of our Hermite Gaussian basis.

It turns out that backscaling makes the difficult problem of choosing a "good" basis even harder for a couple of reasons. The first is that when our eigensolver diagonalizes the complex scaled Hamiltonian, it orthogonalizes our complex scaled eigenfunctions using the "c-norm" $(\phi^{cs}_m|\phi^{cs}_n) = \delta_{mn}$. Unfortunately this doesn't guarantee that our real space wavefunctions are orthogonal and means that we are not allowed to use $\langle\phi^{rs}_m|\phi^{rs}_n\rangle = \delta_{mn}$. What we must do to calculate the norm is exactly the same as we did when calculating the orthogonality matrix for

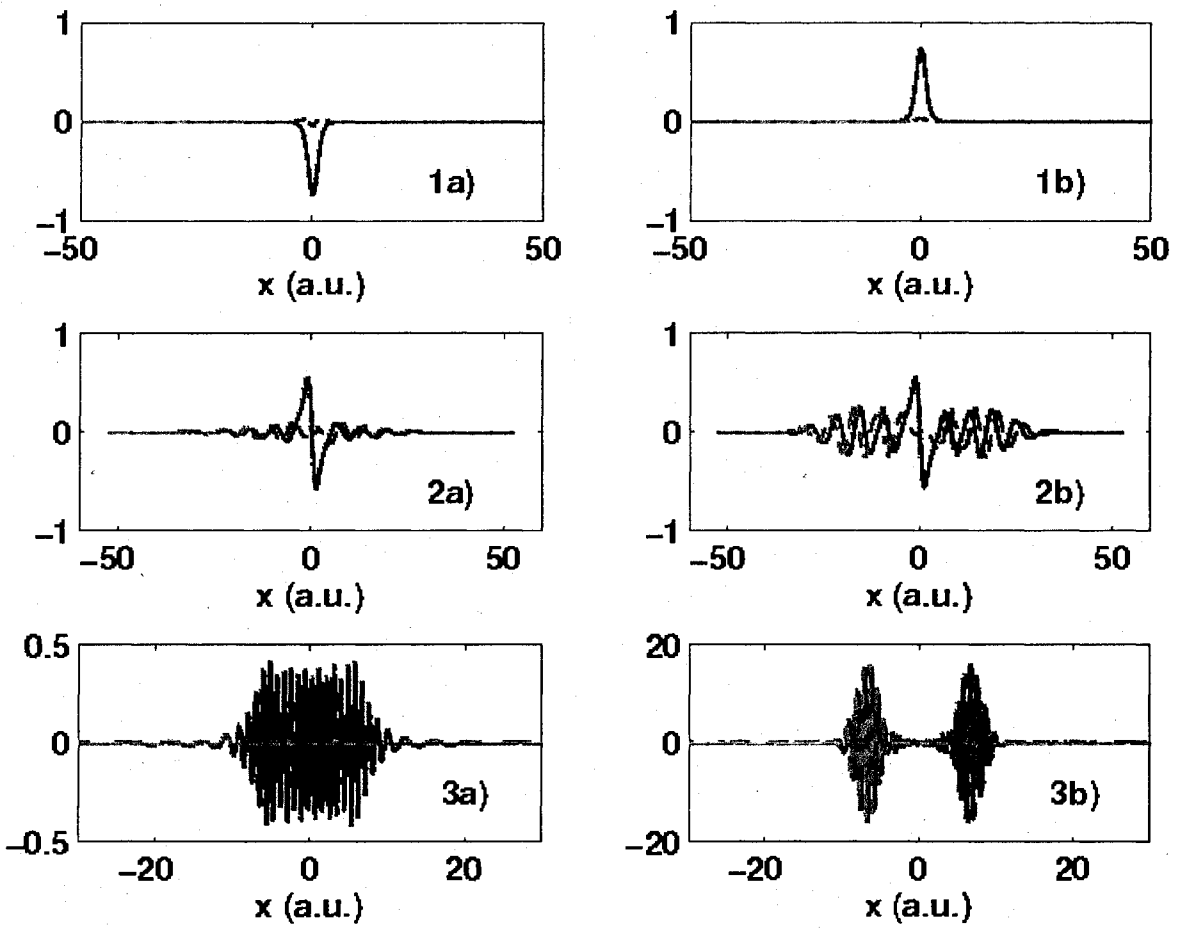

Figure 4.5. A plot of the real (solid lines) and imaginary (dashed lines) parts of the 1) ground state in a) complex scaled space and b) backscaled into real space, 2) resonance state in a) complex scaled space and b) backscaled into real space, 3) a continuum state in a) complex scaled space and b) backscaled into real space. It is clear that while the ground state wavefunction essentially stays the same between the complex scaled and real space, the continuum wavefunction diverges when backscaled. These calculations were done using two basis sets, the first with 50 Hermite Gaussians of width $w_1 = 1$ and the second with 20 Hermite Gaussians of width $w_2 = 5$. All of the states have been normalized in the complex scaled space using the "c-norm", and then backscaled.

solving the generalized eigenvalue problem and calculating a norm with a non-orthogonal basis as in Eq. A.28. We must construct our orthogonality matrix O^{rs}.

To ensure that our real space norm is enforced throughout the calculations, we calculate the Hermitian norm of the real space eigenfunctions

$$\begin{aligned} N_m &= \langle \phi_m^{rs} | \phi_m^{rs} \rangle \\ &= \left(\sum_i c_{mi}^* \left\langle \zeta_i \left(x e^{-i\theta} \right) \right| \right) \left(\sum_j c_{mj} \left| \zeta_j \left(x e^{-i\theta} \right) \right\rangle \right) \\ &= \sum_{ij} c_{mi}^* c_{mj} \langle \zeta_i \left(x e^{-i\theta} \right) | \zeta_j \left(x e^{-i\theta} \right) \rangle \\ &= \sum_{ij} c_{mi}^* c_{mj} O_{ij}^{rs} \end{aligned} \tag{4.6}$$

where $O_{ij}^{rs} = \langle \zeta_i \left(x e^{-i\theta} \right) | \zeta_j \left(x e^{-i\theta} \right) \rangle$ are the matrix elements of the real space orthogonality matrix, and then write our real space eigenfunctions so that they are normalized to unity

$$\phi_m^{rs} = \sum_i \frac{c_{mi}}{\sqrt{N_m}} \zeta_i \left(x e^{-i\theta} \right) \tag{4.7}$$

we then also enforce this norm on our complex scaled eigenfunctions so that

$$\phi_m^{cs} = \sum_i \frac{c_{mi}}{\sqrt{N_m}} \zeta_i \left(x \right) \tag{4.8}$$

The second complication is due to the fast oscillations and incredible divergence of the backscaled wavefunctions. We were required to use Gaussian quadrature to calculate the complex scaled space orthogonality matrix, O^{cs} between non-orthogonal basis functions for our Hermite Gaussian basis sets which was not numerically difficult as our basis functions drop off exponentially (see Appendix A for a more complete explanation and Appendix B for the method of Gaussian quadrature). When we perform backscaling on our Hermite Gaussians they don't decay as $x \to \pm\infty$ but they diverge. This means that our real space orthogonality matrix, O^{rs}, has to constantly sum large negative and positive numbers and as we add more basis functions the calculation becomes numerically much more difficult.

The final complication with backscaling is that as we add more basis functions, when we backscale, our real space basis functions start to become linearly dependent. When this happens we lose the ability to properly describe the problem because we won't have a complete basis (or as complete as is possible with a finite basis). All of these problems mean our calculations are extremely sensitive to the parameters we use, and a lot of work has to go into calculating backscaled wavefunctions.

4.2 Time Dependent Calculations

Having calculated these time independent eigenstates, we would like to be able to use them in time dependent calculations. Our ultimate goal is to be able to perform time dependent calculations to analyze the dynamics of effects like non-sequential ionization and above threshold ionization but we must first characterize our method with a test system to ensure our results are correct. We are most interested in the results we obtain from the complex backscaling method, as these

are the results which will allow us to calculate the dynamics in the real world compared to what we calculate in the complex scaled space. We have derived a set of coupled level equations, Eq. 3.11, and we have also given a method for just simply propagating the wavefunction in time, Eq. 3.20 but these equations need to be tested and compared to time dependent solutions of the non-complex scaled Hamiltonian. To perform these tests we shall use four different methods for calculating the time dependent eigenfunctions.

(i) The first method which was used involved calculating the ground state of the system using the SGR but without any complex scaling. This was done by keeping the same dx as in the complex scaled SGR, but the x range was extended to ± 300 a.u. and 9000 points were used. This Hamiltonian was then used to propagate the system with the time dependent electric field according to Eq. 3.20. The exponential in this equation was approximated as (in a.u.)

$$\begin{aligned} \psi(t+\Delta t) &= \exp(-X)\,\psi(t) \\ &\approx \left[\hat{I} - X + \frac{X^2}{2} - \frac{X^3}{6}\right]\psi(t) \end{aligned} \tag{4.9}$$

where $X = i\Delta t\hat{H}(t+\Delta t)$. We then used $\Delta t = 0.001$ a.u., which gives us convergence in time as long as all the terms in the Hamiltonian are small enough so that $(H_{ij}\Delta t)^3 << 1$. These runs were done so that we could measure ionization simply by measuring the norm in a finite range around the potential, ie

$$N^{ns} = \int_{-a/2}^{a/2} |\Psi^{ns}|^2\, dx \tag{4.10}$$

where N^{ns} is the norm of the real space wavefunction, Ψ^{ns}, calculated when there is no scaling. As the wavefunction propagates out of the system we will see a drop in our norm, and as long as our boundaries are far enough away so that our wavefunction doesn't reflect back into the center of our space before the simulation is finished then this gives a very good measure of our ionization.

(ii) The second method by which the pulses were propagated is very similar to the first, except we use complex scaling in the SGR, and we used all of the same spatial parameters as in the time independent SGR runs for calculating the eigenfunctions. A smaller time step of $\Delta t = 0.0001$ a.u. was required for these runs in order to get convergence. These runs were done so that we could project our field dependent (and hence time dependent) eigenfunctions onto our propagated wavefunction, Ψ^{sgr}. These projections can then be compared to the populations in the states of our coupled level equations to give us confidence in this method and allow us to compare the norm of this system, $N^{sgr} = (\Psi^{sgr}|\Psi^{sgr})$, with the norm from our real space calculations, N^{ns}.

(iii) The third method of calculating our time dependent wavefunction involved solving the coupled level equations developed in Sec. 3.1. The K coefficients were calculated as in Eq. 3.18 using the field dependent eigenstates calculated from the SGR, but it was noticed that particular care must be taken with the symmetry of the eigenstate in question due to the nature of the "c-norm". For instance, if you prepare your system in an antisymmetric, field free state, $\psi(F=0)$ and project on it with the same state at $F = \Delta F$, the overlap you obtain is

$$(\psi(F=\Delta F)\,|\psi(F=0)) = \int_{-\infty}^{\infty} \psi(F=\Delta F)\,\psi(F=0)\,dx \tag{4.11}$$

Then, if you were to calculate $\psi(F=-\Delta F)$, it is natural to assume that switching the values of the wavefunction for positive and negative x should give the wavefunction at $F=\Delta F$. However because our state is anti-symmetric $\psi(-\Delta F)=-\psi(\Delta F)$, and when we project onto our field free wavefunction we obtain

$$\begin{aligned}(\psi(F=-\Delta F)|\psi(F=0)) &= -\int_{-\infty}^{\infty}\psi(F=\Delta F)\,\psi(F=0)\,dx \\ &= -(\psi(F=\Delta F)|\psi(F=0))\end{aligned} \tag{4.12}$$

This means that when calculating the K coefficients we must ensure that the sign of our wavefunction is the same at $\pm\Delta F$ or else we will have a discontinuity in the field dependent K coefficients as we go through $F=0$. Once these were calculated the coupled level equations were propagated for the ground state and the resonance state using Matlab's adaptive step Runge Kutta propagator. The wavefunction calculated using these level equations will be denoted as $\Psi^{le}=\sum_i c_i^{le}\phi_i$ with a norm of N^{le}.

(iv) The final method used to perform time dependent calculations is by using the global basis function method. The equations used to propagate the wavefunction were the same as in Eq. 3.20, but instead of writing the wavefunction as a Taylor expansion and inserting the Schrödinger equation, we can solve the Schrödinger equation directly using Matlab's adaptive step Runge Kutta program. This means that we give the Runge Kutta our initial wavefunction and tell it to propagate it according to (in a.u.)

$$\frac{d\Psi(t)}{dt}=-i\left(H_0+F(t)\,Q(x)\right)\Psi(t) \tag{4.13}$$

Where H_0 is our field free, time independent, complex scaled Hamiltonian, and $F(t)$ is our time dependent field. Note that the wavefunctions that are used for the global basis function propagation are the wavefunctions in complex scaled space with the complex scaled Hamiltonian. When we wish to examine things like the norm or the probability of being in our resonance then we must first write our complex scaled wavefunction, Ψ^{cs} in terms of our complex scaled eigenfunctions, ϕ_i^{cs}, ie $\Psi^{cs}=\sum_i c_i\phi_i^{cs}(x)$. We then use the coefficients c_i to reconstruct our wavefunction in terms of the real space eigenfunctions $\Psi^{rs}=\sum_i c_i\phi_i^{rs}(x)$ and then calculate the norm, $N_{rs}=\langle\Psi^{rs}|\Psi^{rs}\rangle$. This backscaling is crucial and without it there would be no way to connect the wavefunctions in (ii) and (iii) with (i).

In order to characterize the different methods and ensure that they are consistent with each other, laser pulses whose frequency (0.813 a.u.) was resonant with the zero field energy difference between the resonance and the ground state were propagated in each method. The amplitude of the pulses were chosen so that the peak of the field came just up to the first avoided crossing in Fig. 4.2 (ie 0.005 a.u.) and had a Gaussian envelop. The pulse half width at half maximums (HWHMs), τ, of the pulses was $\tau=10\sqrt{\ln 2}$ a.u..

When we use the four methods described above for a pulse with $\tau=20\sqrt{\ln 2}$ a.u. and calculate the respective norms, we obtain Fig. 4.6. It is obvious that the various norms shown all look very different, but fortunately they can all be related to each other. If we use our N^{ns} as a baseline for comparison (the black line in Fig. 4.6), we first see that the norm calculated using $N^{sgr}=(\Psi^{sgr}|\Psi^{sgr})$ (the dashed red line) oscillates rapidly beneath the value of the N^{ns}, but it never actually touches the N^{ns}. There are two reasons for this; The first is that when we calculate N^{ns} we must choose our range over which to integrate a. We must choose a large enough so that before the pulse propagates through the system we have $N^{ns}=1$. However, the

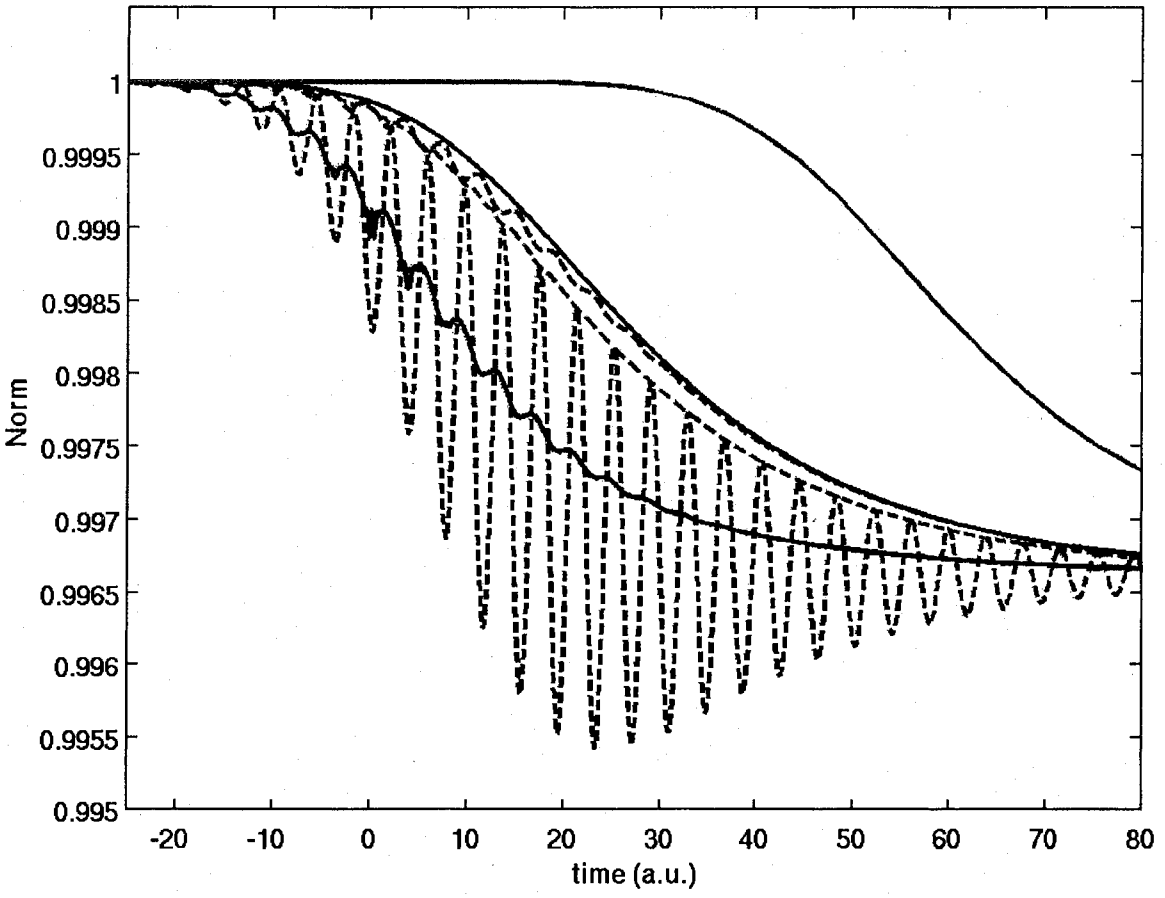

Figure 4.6. A plot of norm of our wavefunction from various methods. 1) N^{ns} from method (i) was calculated by choosing $a = 6$ a.u. in Eq. 4.10 and is shown as a solid black line. 2) N^{le} from method (iii) is shown by calculating $N^{le} = \left|\sum_i = \left(c_i^{le}\right)^2\right|$ and is shown as the solid blue line (underneath the solid red line). 3) N^{sgr} was calculated in two ways. The first was found by taking our time dependent wave function and calculating $N^{sgr} = (\Psi^{sgr}|\Psi^{sgr})$ which is shown as the dashed red curve. Due to the rotating energy terms when we write this "c-norm" what we are really calculating is $|(\Psi^{sgr}|\Psi^{sgr})| = \left|\sum_i (c_i^{sgr})^2 \exp(-2iE_i t)\right|$. When we take out the rotating terms, $\exp(-2iE_i t)$, within the norm by projecting the field dependent eigenstates from the SGR method and subtract the energy dependent rotation we obtain $N^{sgr}\sum_i (c_r^{sgr})^2$ which is the solid red line. 4) When we calculate the backscaled norm, N^{rs}, we obtain the solid green line. This norm has the same shape as N^{ns} except that it is shifted in time. We also calculate our norm in the complex scaled space from method (iv) (dashed green line) and see that it acts as an envelop for our N^{sgr} 5) If we were to incorrectly calculate our norm from method (ii) as $\langle\Psi^{sgr}|\Psi^{sgr}\rangle$ then we would obtain the dashed blue curve.

larger we make this integration range, the longer it takes for our pulse to propagate out of the system hence the decay is shifted in time. If we were to shift our N^{ns} back in time, we would find that the peaks of the N^{sgr} curve would just touch the N^{ns} curve. The reasons for the oscillations becomes apparent when we write our SGR wavefunction as a superposition of the eigenfunctions $\Psi^{sgr} = \sum_i c_i^{sgr} \phi_i^{sgr} \exp(-iE_i t)$and use the "c-norm" to calculate N^{sgr},

$$\begin{aligned} N^{sgr} &= |(\Psi^{sgr}|\Psi^{sgr})| \\ &= \left| \sum_i \left(c_i^{sgr}\right)^2 (\phi_i^{sgr}|\phi_i^{sgr}) \exp(-2iE_i l) \right| \\ &= \left| \sum_i \left(c_i^{sgr}\right)^2 \exp(-2iE_i t) \right| \end{aligned} \tag{4.14}$$

We immediately see that we have phase terms which will mix when we calculate our norm. Measuring the frequency of the oscillations is direct proof of this as we find that the frequency is, $\omega = 2(\mathrm{Re}(E_r) - \mathrm{Re}(E_g))$, where $\mathrm{Re}(E_{g/r})$ are the real parts of the energy of the ground and resonance state. Since we know the time dependent energy levels, we can remove this rotating term to calculate

$$\begin{aligned} N^{sgr} &= \left| \sum_i \left(c_i^{sgr}\right)^2 (\phi_i^{sgr}|\phi_i^{sgr}) \right| \\ &= \left| \sum_i \left(c_i^{sgr}\right)^2 \right| \end{aligned} \tag{4.15}$$

When we do this, we find that this norm (solid red line) and the norm from the level equations (the solid blue line)

$$\begin{aligned} N^{le} &= \left(\Psi^{le}|\Psi^{le}\right) \\ &= \left| \sum_i \left(c_i^{le}\right)^2 \right| \end{aligned} \tag{4.16}$$

match very well, but they look even less like the N^{ns}. This is because, even though we don't have our rotating energy terms, our applied electric field is rotating the individual c_i's for each level, so in Eq. 4.16 we there are still getting mixing between phases of the states, but we are unable to extract them. Also, if we try incorrectly calculating $N^{sgr} = \sum_i |c_i^{sgr}|^2$ (the dashed blue line) we see the same type of unphysical oscillations that were previously observed by Gilary *et al.*

Finally, we can tie in the norm obtained from method (iv) with complex backscaling with all of the previous calculations for the norm. First, we had the wavefunction written in complex scaled space and propagated, but with the normalization enforced in real space. We could then look at the norm in complex scaled space which is $N^{cs} = (\Psi^{cs}|\Psi^{cs})$ (shown as the dashed green line) or the norm in real space $N^{rs} = \langle \Psi^{rs}|\Psi^{rs}\rangle$ (the solid green line). The first thing that we notice is that the N^{cs} is almost exactly the envelop of N^{sgr}. This shows that while our "c-norm" gives a very good measure of the norm in complex scaled space, the fact that we don't see the same oscillations as in the N^{sgr} or the N^{le} shows our normalization condition must have an effect on the norm in complex scaled space. When we examine the N^{rs}, we see a curve that has the exact same shape as our N^{ns} from method (i) but is shifted much farther in time. The reason for this shift was only discovered by examining the time dependent probability distribution in real

space from method (iv), $|\Psi^{rs}|^2$, and examining the eigenfunction basis we use. What we see in the time propagation is that during the laser pulse there is a slow build up of probability away from the nucleus which slowly propagates outward not unlike what we see in method (i). However, once our probability comes to the end of the extent of our basis functions, we immediately see the probability ejected as the outgoing boundary condition is explicitly enforced. This means that our backscaling recreates the same scenario as in method (i) where we only calculate the norm when it is within the boundaries of some "space", either defined by our integration region as in method (i) or defined by our eigenfunction equation as in method (iv). Thus, in Fig. 4.6 the only norms we can associate with the physical world are 1) the norm calculated using method (i) in real space (the solid black line) and 2) the backscaled norm (the solid green line).

Since we have the the eigenfunctions, it would be interesting to compare methods (ii) - (iv) in terms of how they predict probabilities in a given state. We can see from Fig. 4.7 a), that all of the methods predict the same population in the ground state regardless of using the level equations, or projecting with our ground state using SGR. The global basis function method also gives the same probability in both complex scaled space and backscaled space. However in Fig. 4.7 b) we see something very interesting. We predict the exact population in the resonance using the level equations, projecting with our ground state using SGR, and using the global basis set method in complex scaled space. However, when we look at the probability of being in the backscaled state that corresponds to the complex scaled resonance, we see it appears there isn't any resonance at all (dot-dashed green line). What happens is that after backscaling because there is such strong mixing due to the orthogonality matrix, O^{rs}, our population is transferred to another state (the solid green line). This is a major issue if we plan to use this method as a way of tracking the path an electron takes as it is ionized, and thus far we have been unable to solve it. If our resonance state is a single state in the complex scaled domain, but then is spread out as a superposition of all of our basis states in the real domain then we can identify the dynamics with a single state (ie, the first excited or the second excited).

To further test our backscaling method, we tried a higher pulse amplitude of $F = 0.025$ a.u., and compared it with the backscaling method for $F = 0.005$ a.u. (Fig. 4.8). We see that for a field of 0.005 a.u. we don't excite any of the continuum states significantly compared to the resonance, and when we do this our $N^{cs} = (\Psi^{cs}|\Psi^{cs})$ and $N^{rs} = \langle\Psi^{rs}|\Psi^{rs}\rangle$ are reasonably behaved. However, when use a field of 0.025 a.u. we see that our real space norm is again reasonably behaved but our N^{cs} oscillates wildly about unity in the region where the field is present. When we look at the resonance and continuum populations, we see that these oscillations occur in the same region where we have an exchange of population between the resonance and the continuum levels. This population exchange is due to the avoided crossings as seen in Fig. 4.2 which we trace through with each field halfcycle. We also notice in the inset of 2a) of Fig. 4.8 that when we obtain these population exchanges our ionization rate oscillates. This is again due to the population exchange between the resonance and continuum states, but we can see from Fig. 4.3 that our ionization rate is at its highest when we are in our resonance and the field is centered around $F = 0$ a.u., and then when we are put into the continuum our ionization rate drops and, depending on the continuum state, can become positive.

Using complex backscaling we have shown that we can accurately describe the dynamics of the system in a space that doesn't require the "c-norm". While these calculations are difficult to perform, we have been able to show that they can be much more robust than the "c-norm" which is traditionally used. While we have yet to show any new physics this method has great potential for future use in describing intense field dynamics in a variety of ways. For instance, investigating the effects of a short, intense, infra-red pulse along with an attosecond XUV pulse to see how the larger field values can change the ionization, or by using extremely short (ie two cycle) infra-red

pulses and examining the nonlinearities created by such a pulse. Also, by switching to a form of exterior complex scaling we could examine a much broader class of potentials.

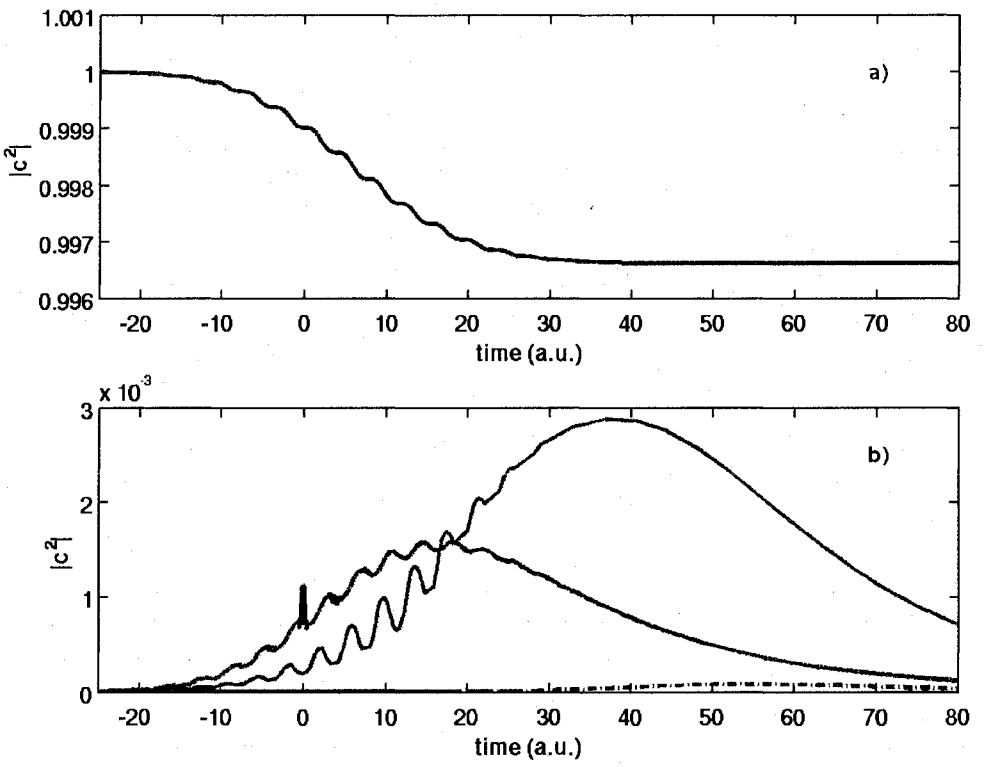

Figure 4.7. A plot of the populations in a) the ground state, and b) in the resonance state as a function of time. The blue lines are the results from the coupled level equations of method (iii), the red lines are the results from projecting our field dependent eigenstates on the wavefunction propagated via method (ii) the dashed green lines are the results of using the global basis function method and the solid green lines are the results when we backscale. The green dot-dashed line in b) shows the amount left in the backscaled state that corresponds to the complex scaled resonance but lost all probability due to the strong mixing when we backscale. In a) all four lines are directly on top of each other, and in b) the red, and blue solid lines as well as the green dashed line are all directly on top of each other, ie all of the complex scaling calculations predict the same result.

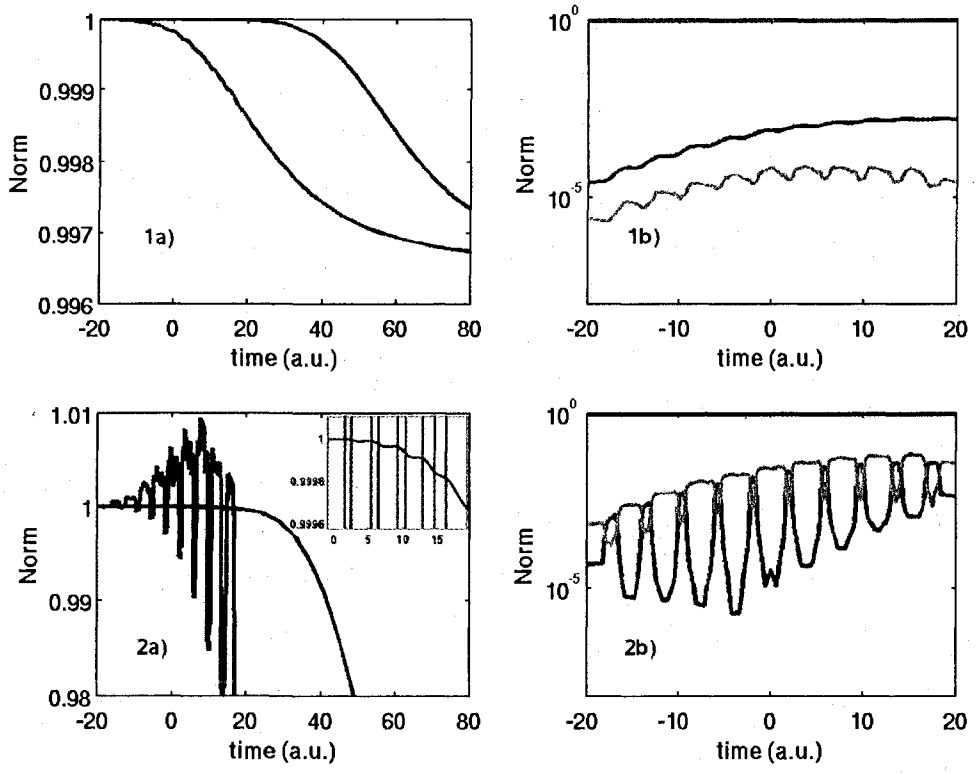

Figure 4.8. 1) For a field of $F = 0.005$ a.u., we plot a) the norm in complex scaled space using $N^{cs} = (\Psi^{cs}|\Psi^{cs})$ (the red curve), and the norm in real space $N^{rs} = \langle\Psi^{rs}|\Psi^{rs}\rangle$ (the blue curve) b) the amount in the ground state in complex scaled space (the red line), the amount in the resonance in complex scaled space (the blue line), and the amount in continuum, $\left|\sum_{i\neq g,r}(c_i^{cs})^2\right|$ in complex scaled space (the green line). 2) For a field of $F = 0.025$ a.u., we plot a) the norm in complex scaled space using $N^{cs} = (\Psi^{cs}|\Psi^{cs})$ (the red curve), and the norm in real space $N^{rs} = \langle\Psi^{rs}|\Psi^{rs}\rangle$ (the blue curve), inset shows a zoomed region of the N^{rs} b) the amount in the ground state in complex scaled space (the red line), the amount in the resonance in complex scaled space (the blue line), and the amount in continuum, $\left|\sum_{i\neq g,r}(c_i^{cs})^2\right|$ in complex scaled space (the green line).

Chapter 5

2D Calculations

Having developed our 1D model and examined the effects of the norm, it would be useful to perform calculations in 2D for more concrete systems. Thus far we have only developed the multi-level equations and the SGR for 2D calculations but it would still be educational to examine how the methods we have developed can be applied despite not being able to backscale. Our interest in complex scaling began as a diagnostic tool for the multi-configuration time dependent Hartree Fock (MCTDHF) method developed by C. McDonald for his Master's thesis[3]. The MCTDHF is capable of solving the fully correlated dynamics of a two dimensional multi electron system in a time dependent field, but extracting useful information from the calculations can be extremely difficult. The particular problem that was being investigated with MCTDHF was the effects of non-sequential ionization, where a short, intense, infra-red pulse is incident on a two electron system such as N_2. In the first half-cycle of the pulse one electron is ionized and is pulled from the nucleus by the field. As the pulse changes sign, the electron is accelerated back towards the nucleus where it interacts with the bound electron and both electrons can be ejected. Due to the strongly correlated dynamics of the system, it is difficult to interpret the results into a clean model for the dynamics. Our hope for the complex scaling method is that once backscaling is possible, we can calculate the field dependent eigenstates of the single electron system of N_2^+ and use these to interpret the dynamics of the full two electron system. To this end, we shall examine the eigenstates of N_2^+ in terms of the electric field and perform time dependent calculations using these states.

5.1 Time Independent Calculations

For calculating our eigenfunctions we used the diatomic potential

$$V(x,y) = \frac{-Z}{\sqrt{(x-a)^2 + y^2 + sm^2}} + \frac{-Z}{\sqrt{(x+a)^2 + y^2 + sm^2}} \tag{5.1}$$

where $Z = 1$ was used for the charge on each nucleus. The separation of the nuclei, $2a$, was determined by calculating the ground state energy for this potential and then comparing it with the ionization potential of N_2^+, and the smoothing parameter sm was chosen so that the energy difference between the ground state and the first excited state matched the resonance of these two states for N_2^+. This gave us a spacing of $2a = 2.0859$ a.u. and a smoothing of $sm = 0.7129$ a.u. These values were found by calculating the eigenvalues without performing any complex scaling and with a uniform grid spanning $[-50\ 50]$ and a spacing of $dx = dy = 0.4$ a.u.

Because of the poles in the complex plane for our potential we are prohibited from using UCS. We decided to use SMECS and found that the parameters that seemed to give the best convergence were $\theta = 0.4$, $x_r = 2$ a.u., $x_0 = 30$ a.u., $y_r = 2$ a.u., and $y_0 = 30$ a.u.. The form of our smoothing function (which is the same in both the x and y direction) from equation 2.19 is

$$g(\alpha) = \frac{1}{4}\left(2 + 3\alpha - \alpha^3\right) \tag{5.2}$$

where $\alpha = \frac{x - x_0}{x_r}$ 2.19. The function $g(\alpha)$ was chosen in the same manner as Rescigno *et. al.* [11] as the lowest order polynomial that gives $g(-1) = 0$, $g(1) = 1$, $g'(-1) = 0$ and $g(1) = 0$ in order to ensure a smooth q and q' at $x = x_0 - x_r$ and $x = x_0 + x_r$. Our eigenstates were calculated for various electric field values between $F = 0$ and $F = 0.03$, but due to the long simulation times involved in calculating the eigenstates for a single electric field value a relatively coarse step size in the field was used. The eigenstates were still tracked as described in Sec. 4.1.1 and when the overlap between eigenstates for $F = F_0$ and $F = F_0 + \Delta F$ became ambiguous the step size was halved until the eigenstate could be properly tracked without ambiguity.

The ground and first fourteen excited states are given in Figs. 5.1 - 5.4 for the field free case and with electric fields of $F = 0.01$ a.u. and $F = 0.02$ a.u. Fig. 5.5 shows how the energy levels move within the potential at those electric field values, and Fig. 5.6 shows the energies of the fifteen states as a function of electric field. There is an amazing wealth of information contained within these figures. First, it is easy to see that when our states have their probability almost entirely centered around the nucleus in Figs. 5.1 - 5.4 we see that in Fig. 5.5 the energy of the given state is still within the well, and thus the state is bound. When our state starts to become extended in space it becomes a resonance and we see that it's energy is well above the barrier (a very good example is 4b) of Fig. 5.2 showing the seventh excited state and looking at it's energy in 2b) of Fig. 5.5). Then, as the electric field is further increased our states lose all of their probability of being found near the nucleus and their energy dips below the level of the barrier on the outside. These are states that have been turned completely into continuum states by the electric field.

Fig. 5.6, which shows the energy levels as a function of the field, illustrates these effects further as we can see that when our states are still bound their energies are practically level with their field free energy levels. Then, as the potential barrier dips below an energy level, the energy level starts to curve down in the shape of a parabola as our state becomes a resonance. When the energy level of our state becomes completely linear in terms of our electric field, then our state is truly a continuum state.

We can also see some interesting features as we increase the electric field. For instance, it appears that the orientation of the symmetry of the state has a large effect on how long the state stays bound to nucleus. For instance, states whose symmetries are perpendicular to the field such as the fourteenth excited state (plot 3 of Fig. 5.4), seem to hold onto their resonance characteristics longer than states which are parallel to the field such as the thirteenth excited state (plot 2 of Fig. 5.4). This is further illustrated in Fig. 5.6, where these states have been highlighted in yellow and green.

5.2 Time Dependent Calculations

For our time dependent calculations, we wanted to try and perform simulations to connect to the MCTDHF calculations. The MCTDHF calculations were done with a two cycle 800 nm (0.0456 a.u.) laser pulse with a peak amplitude of $F = 0.03$ a.u.. We know that in non-sequential

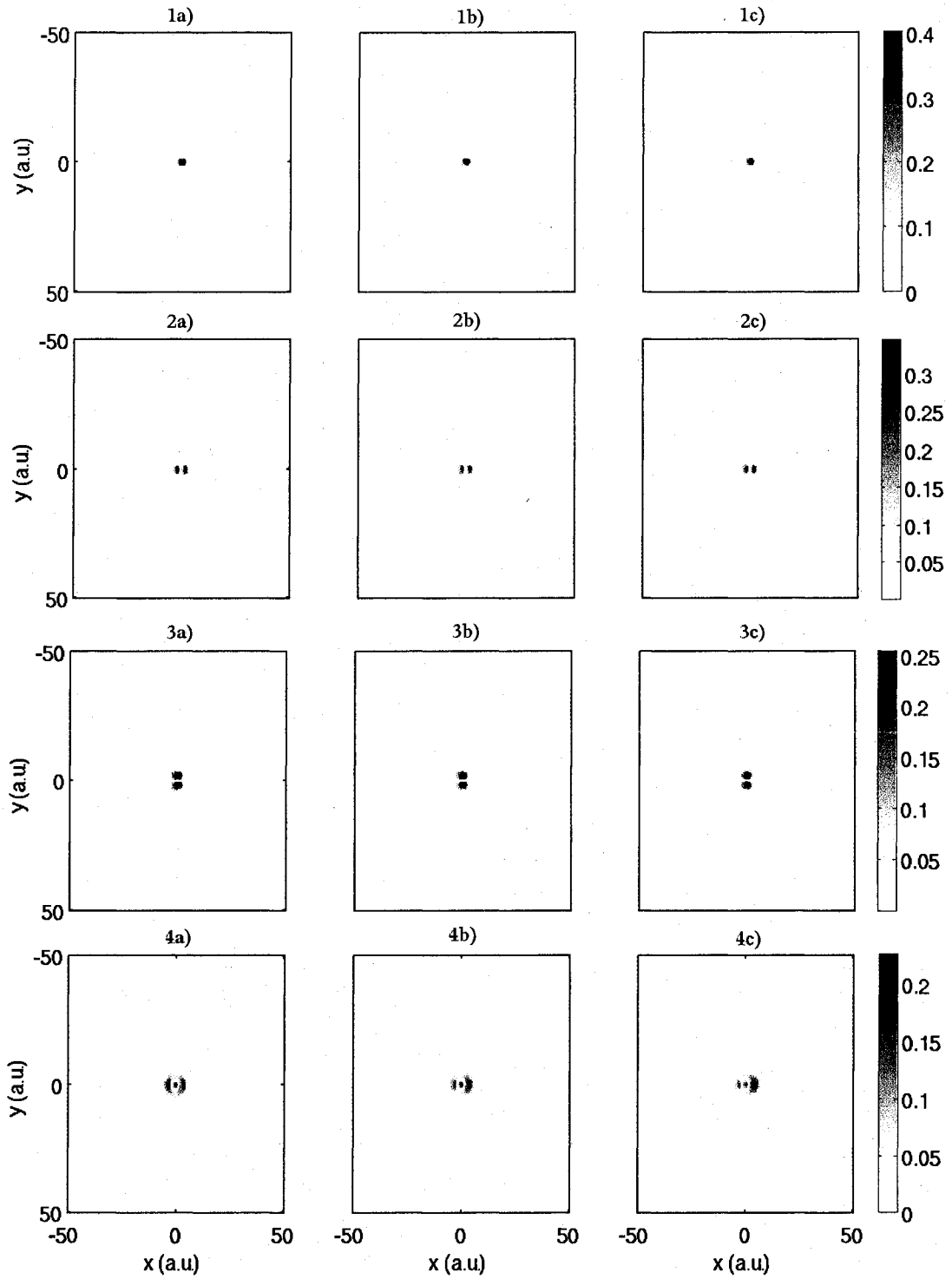

Figure 5.1. Plot of $|\phi^2|$ for the 1) Ground state for electric fields of a) $F = 0$ a.u., b) $F = 0.01$ a.u., and c) $F = 0.02$ a.u. 2) First excited state for electric fields of a) $F = 0$ a.u., b) $F = 0.01$ a.u., and c) $F = 0.02$ a.u. 3) Second excited state for electric fields of a) $F = 0$ a.u., b) $F = 0.01$ a.u., and c) $F = 0.02$ a.u. 4) Third excited state for electric fields of a) $F = 0$ a.u. b) $F = 0.01$ a.u., and c) $F = 0.02$ a.u.

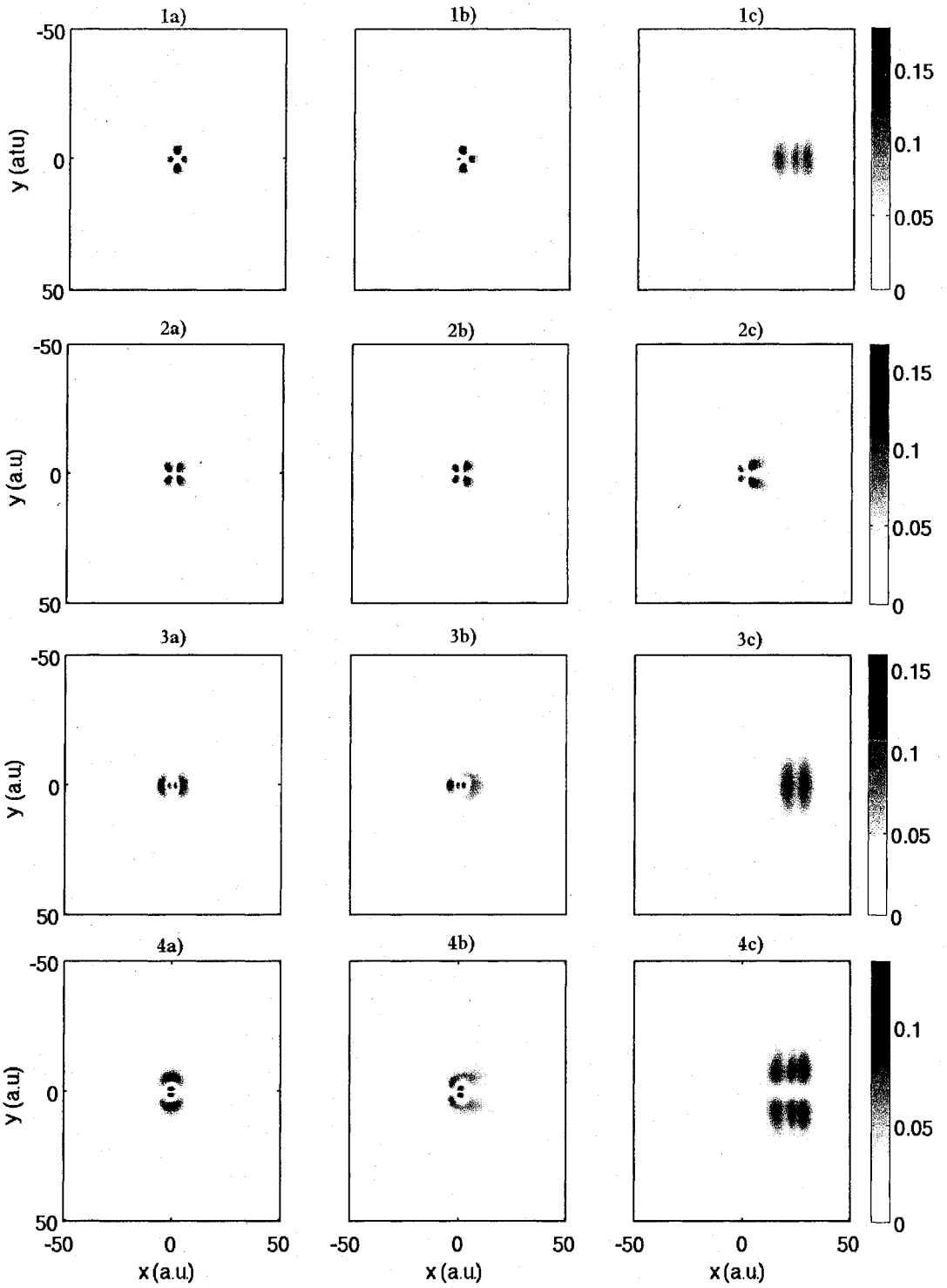

Figure 5.2. Plot of $|\phi^2|$ for the 1) Fourth excited state for electric fields of a) $F = 0$ a.u., b) $F = 0.01$ a.u.., and c) $F = 0.02$ a.u. 2) Fifth excited state for electric fields of a) $F = 0$ a.u., b) $F = 0.01$ a.u., and c) $F = 0.02$ a.u. 3) Sixth excited state for electric fields of a) $F = 0$ a.u., b) $F = 0.01$ a.u., and c) $F = 0.02$ a.u. 4) Seventh excited state for electric fields of a) $F = 0$ a.u. b) $F = 0.01$ a.u., and c) $F = 0.02$ a.u.

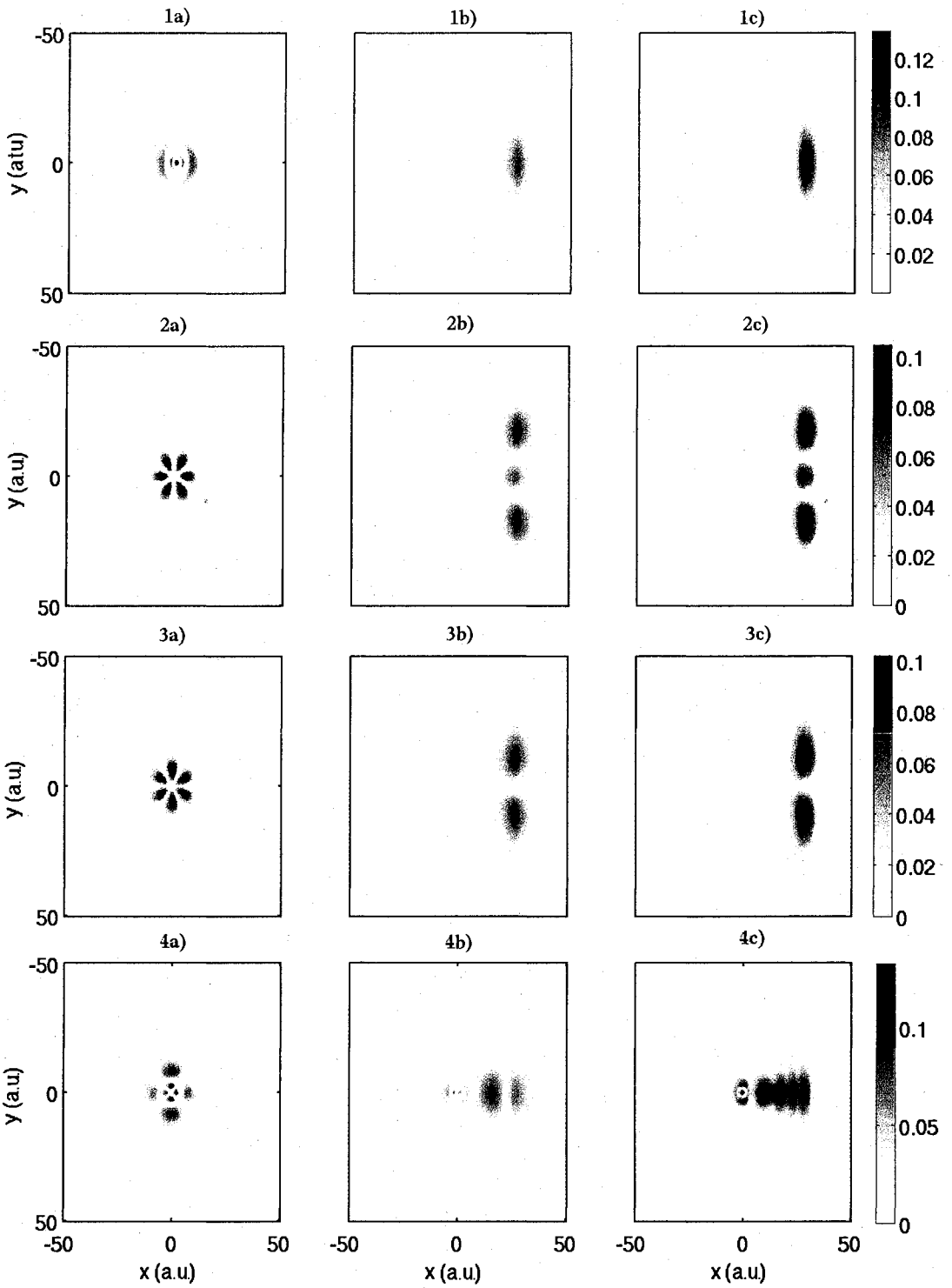

Figure 5.3. Plot of $|\phi^2|$ for the 1) Eighth excited state for electric fields of a) $F = 0$ a.u., b) $F = 0.01$ a.u., and c) $F = 0.02$ a.u. 2) Ninth excited state for electric fields of a) $F = 0$ a.u., b) $F = 0.01$ a.u., and c) $F = 0.02$ a.u. 3) Tenth excited state for electric fields of a) $F = 0$ a.u., b) $F = 0.01$ a.u., and c) $F = 0.02$ a.u. 4) Eleventh excited state for electric fields of a) $F = 0$ a.u. b) $F = 0.01$ a.u., and c) $F = 0.02$ a.u.

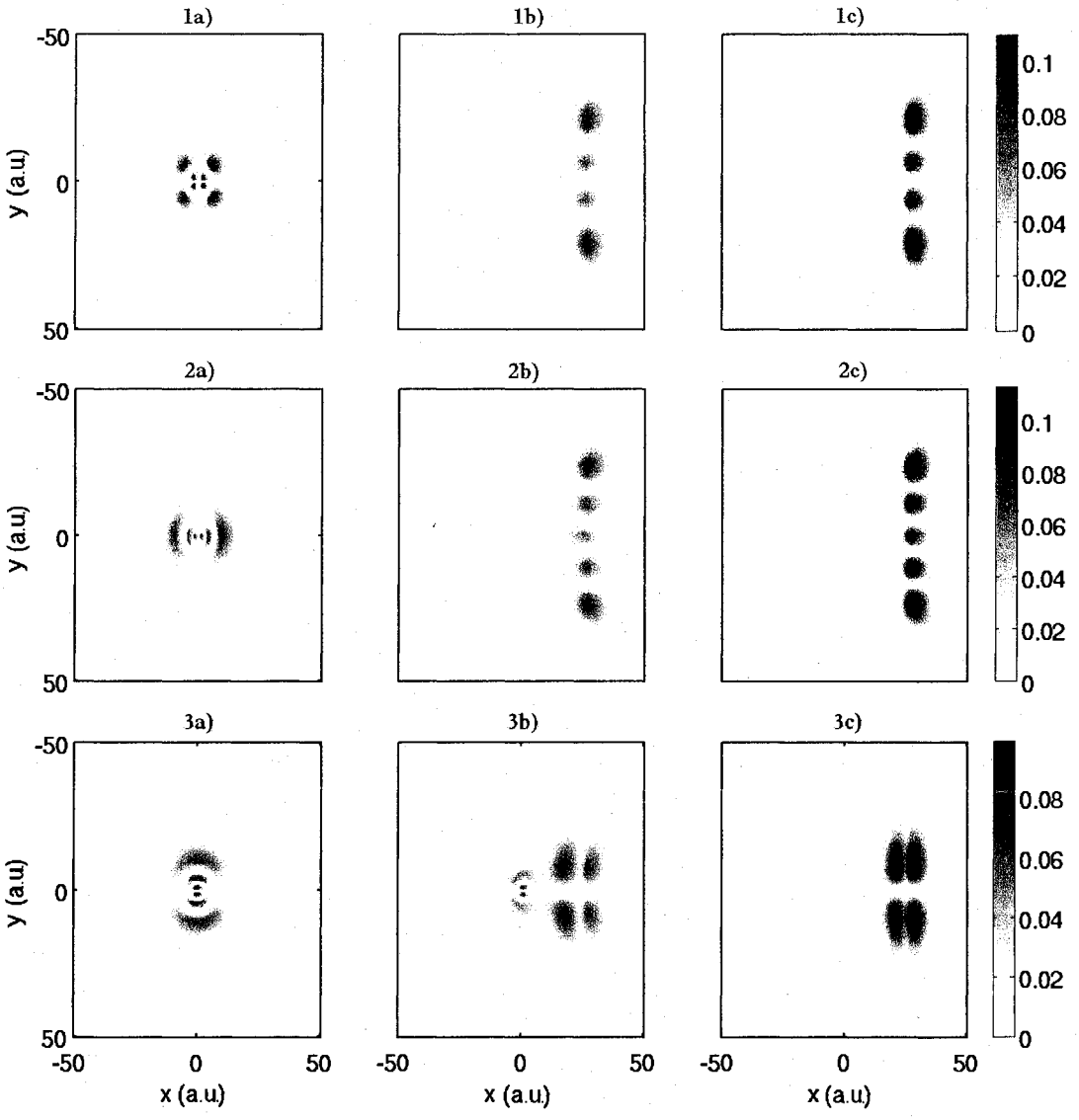

Figure 5.4. Plot of $|\phi^2|$ for the 1) Twelfth excited state for electric fields of a) $F = 0$ a.u., b) $F = 0.01$ a.u., and c) $F = 0.02$ a.u. 2) Thirteenth excited state for electric fields of a) $F = 0$ a.u., b) $F = 0.01$ a.u., and c) $F = 0.02$ a.u. 3) Fourteenth excited state for electric fields of a) $F = 0$ a.u., b) $F = 0.01$ a.u., and c) $F = 0.02$ a.u.

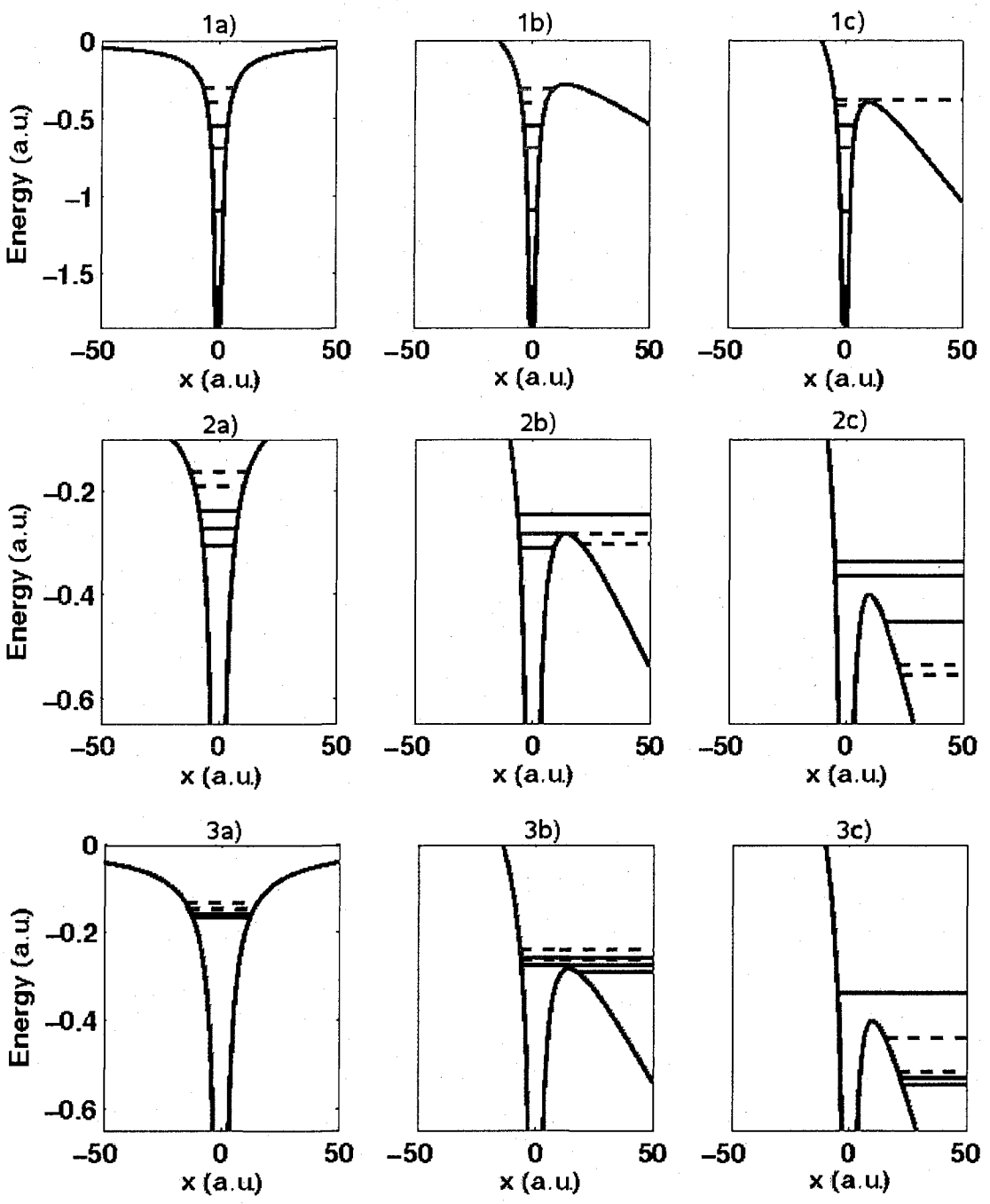

Figure 5.5. Plots of the potential well for the field values used in Figs. 5.1 - 5.4, and the energy levels of the eigenstates at these field values. 1) The energy levels for the ground state (solid red line), first excited state (solid green line), second excited state (solid black line), third excited state (dashed red line) and fourth excited state are shown for a) $F = 0$ a.u. b) $F = 0.01$ a.u. c) $F = 0.02$ a.u. 2) The energy levels for the fifth excited state (solid red line), sixth excited state (solid green line), seventh excited state (solid black line), eighth excited state (dashed red line) and ninth excited state are shown for a) $F = 0$ a.u. b) $F = 0.01$ a.u. c) $F = 0.02$ a.u. 3) The energy levels for the tenth state (solid red line), eleventh excited state (solid green line), twelfth excited state (solid black line), thirteenth excited state (dashed red line) and fourteenth excited state are shown for a) $F = 0$ a.u. b) $F = 0.01$ a.u. c) $F = 0.02$ a.u.

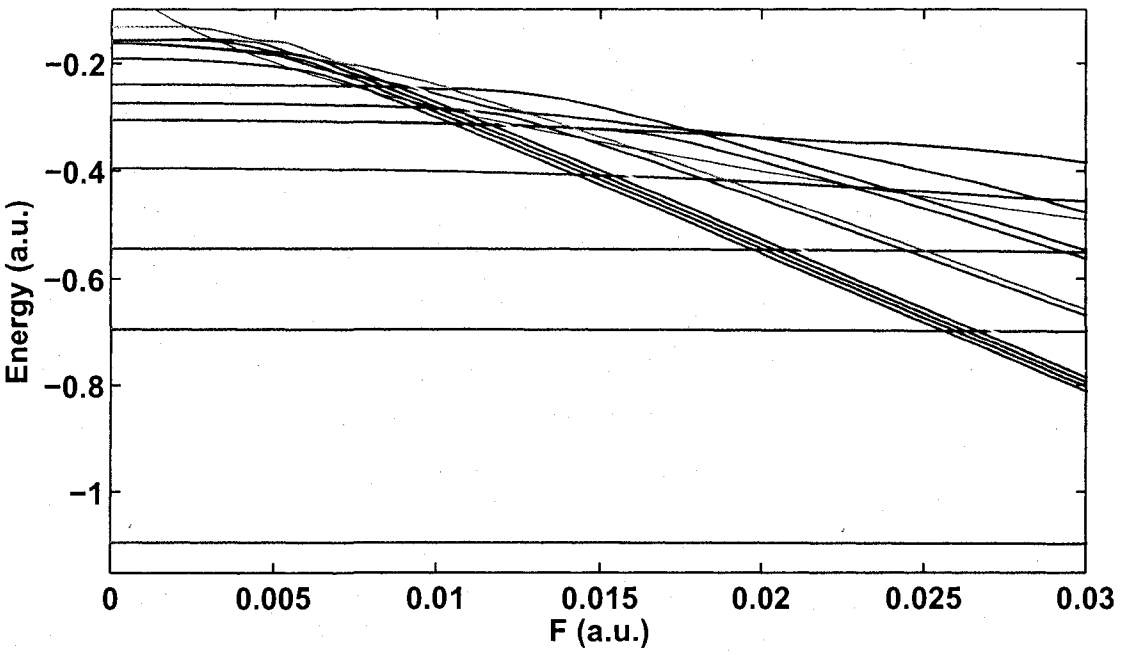

Figure 5.6. Plot of the first fifteen energy levels of N_2^+ as a function of electric field (blue lines). The thirteenth excited state (the yellow line), and the fourteenth excited state (the green line) have been highlighted to show the effects of symmetry. The height of the potential barrier is shown as a function of field (red line).

ionization, on the second half-cycle of the pulse, when the amplitude of the electric field is reversed, the first electron is accelerated back into the ion-electron core and can excite the second electron into a higher state, or completely ionize it. We wish to examine the dynamics of the second electron, so we simulate this excitation by starting the electron in the middle of the field in a field dressed excited state and then propagate the laser pulse through the rest of the field. By starting the simulation in middle of the field with the electron in an excited state we assume that the first electron has already come back to the nucleus, shared energy with the bound electron, and then left the nucleus with the second electron in an excited state.

In each of our simulations we started the electron in the first excited state. We used only two of the methods of propagating the system that we used in the 1D case: method (ii), propagating the state with the complex scaled version of Eq. 3.20 in the SGR and method (iii), the coupled level equations. The real space version of Eq. 3.20 (method (i)) was not performed because of the memory issues involved in propagating in a space large enough such that the wavefunction doesn't reflect back into the nucleus and the global basis function method (method (iv)) has not yet been developed in 2D. In the coupled level equations we solved the equations using only the first eight eigenfunctions and then again with the full 15 eigenfunctions. This was done to see the effect the higher levels had on the populations transferred between the lower states. The

coupled level equations used Matlab's adaptive Runge Kutta solver and the K coefficients were calculated in the same manner as described in Sec. 4.2, where the symmetry of the states was taken into consideration. When the system was propagated according to Eq. 3.20 the same spatial parameters were used as in the 2D time independent calculations and the time step was $dt = 0.01$ a.u..

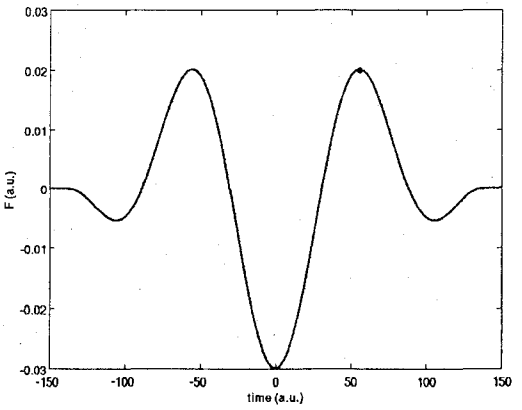

Figure 5.7. The time dependent electric field in which our eigenstate was propagated, and the red dot indicates the point in the field where we start our state, and then after which we propagate.

Fig. 5.7 shows the time dependent field used propagate the eigenstate as well as where we assumed the electron was promoted to the first excited state. Because we started in the first excited state, there are states which have a vanishing K coefficient due to symmetry reasons and don't contribute to the dynamics of the system. Figs. 5.8 and 5.9 show the dynamics that are obtained when we start at the field value indicated in Fig. 5.7. We have only included in the figures the states which had a finite K coefficient with the first excited state even though these states were kept in the level equations. Within a) of Fig. 5.8 we have plotted the populations, $N^{sgr} = |(\Psi^{sgr}|\Psi^{sgr})|$ and $N^{le} = \left|\sum_i \left(c_i^{le}\right)^2\right|$, along with the populations in the first excited state. N^{sgr} was found to be the same regardless of whether or not we took out the rotations due to the energy terms which show up so prominently in Fig. 4.6 because the populations in our other states are so small compared to our initial excited state. We see again the issue of the "c-norm" in a) of Fig. 5.8 as the population within the first excited state is predicted to be higher than the total population of the system. Physically this is impossible as the norm should contain all of the populations of all of the states but the interference we gain by using the "c-norm" means it is possible to have a norm that is smaller than the population in an individual state.

The populations in the ground, first and third excited were found to have very good agreement between the SGR method and the level equations. It is only when we get to the fourth excited state that we see a deviation. If we take our SGR method as our baseline, we need to examine what happens in our level equations. It turns out that the in the region where the populations begin to deviate our electric field passes through $F = 0.01$ a.u.. Examining figure 5.6 shows that in this region our fourth excited state has multiple other energy states crossing with it. Thus, when the K coefficients are calculated from Eq. 3.18 we have a vanishing denominator but still a finite probability in the dipole moment, $(\psi_j(F)|\, x\, |\psi_i(F))$. The value of the all of the

field free K coefficients is of order 1, but when these energy crossings occur, the K coefficients climb to around 500 a.u.. When examining the number of eigenfunctions used, it appears that adding more eigenfunctions may alleviate this problem, especially when we examine the sixth excited state. For higher eigenstates we get even worse agreement between the methods, but that is to be expected given the density of the eigenstates at the higher energy levels and the fact that we would need many more upper levels to properly examine the dynamics at the lower levels.

Initial calculations done by starting the pulse at the first node of the field before the red dot in Fig. 5.7, at a time of about 30 a.u., show a similar behavior of when $F = 0.01$ a.u. is reached, our results all of a sudden deviate and the dynamics of the higher states is completely changed. The zero denominator is the cause of the problem but there are other factors that are compounding the problem. One major difference between UCS and SMECS is that in UCS, when we have a resonance or a bound state it is very localized around the potential, whereas the continuum states have a vanishing probability of being near the potential. Thus when we calculate the K coefficients our $(\psi_j(F)|\, x\, |\psi_i(F))$ term vanishes much faster than the denominator. When we perform any type of exterior complex scaling, because there is no difference between complex scaling and real space in the region of the potential our bound and resonance states mix very strongly with the continuum when the electric field is present and is the reason why our $(\psi_j(F)|\, x\, |\psi_i(F))$ term doesn't vanish as quickly as in UCS.

While this has serious consequences for our multilevel equations, it makes developing the global basis function method and backscaling even more important for 2D SMECS. Our global basis function method, like the SGR, should properly recreate the dynamics as we are just propagating the field using the Hamiltonian, and don't have to worry about what these K coefficients are doing. In fact, implementing backscaling and then calculating the K coefficients in the backscaled space may be the solution to being able to fully describe the dynamics using the multi-level equations.

The 2D calculations we have performed will act as a good starting point for further developing our complex scaling method as a tool to be used to analyze more complex systems. The results for the time independent calculations already show the power of using this method to describe a system by allowing us to examine the effects of applying an intense field. Since we cannot yet properly calculate our norm in such a system extracting quantitative values from calculations is not yet possible, but the qualitative information is still very useful.

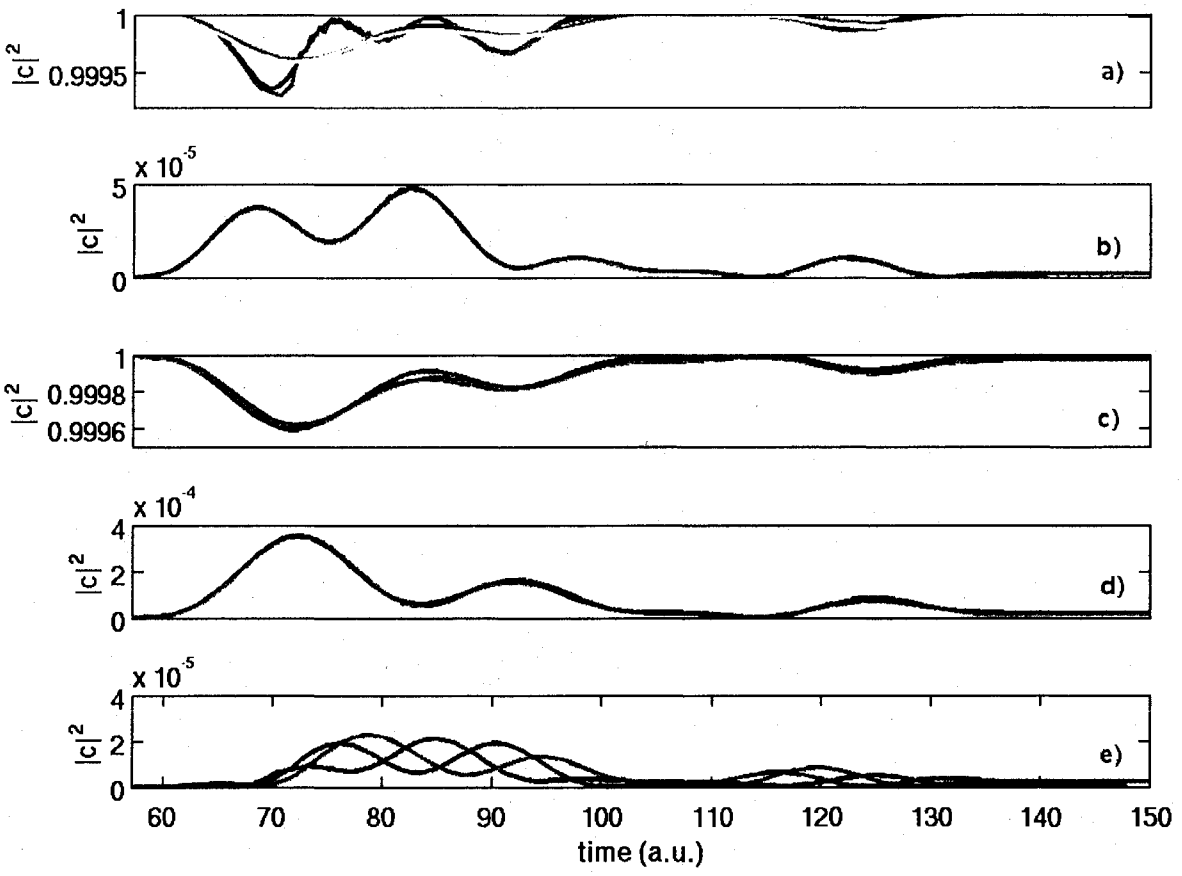

Figure 5.8. Plots of the populations in various states. a) The norms, N^{sgr} (green) and N^{le} (blue) of the system as well as the populations in the first excited state for the SGR $|(\phi_1^{sgr}|\phi_1^{sgr})|$ (yellow) and for the level equations with 15 eigenfunctions $|(\phi_1^{sgr}|\phi_1^{sgr})|$ b) the populations in the ground state for the SGR, $|(\phi_0^{sgr}|\phi_0^{sgr})|$, (red) and for the level equations, $\left|(\phi_0^{le}|\phi_0^{le})\right|$, with 15 eigenfunctions (blue) and 7 eigenfunctions (green) c) the populations in the first excited state for the SGR, $|(\phi_1^{sgr}|\phi_1^{sgr})|$, (red) and for the level equations, $\left|(\phi_1^{le}|\phi_1^{le})\right|$, with 15 eigenfunctions (blue) and 7 eigenfunctions (green) d) the populations in the third excited state for the SGR, $|(\phi_3^{sgr}|\phi_3^{sgr})|$, (red) and for the level equations, $\left|(\phi_3^{le}|\phi_3^{le})\right|$, with 15 eigenfunctions (blue) and 7 eigenfunctions (green) e) the populations in the fourth excited state for the SGR, $|(\phi_4^{sgr}|\phi_4^{sgr})|$, (red) and for the level equations, $\left|(\phi_4^{le}|\phi_4^{le})\right|$, with 15 eigenfunctions (blue) and 7 eigenfunctions (green)

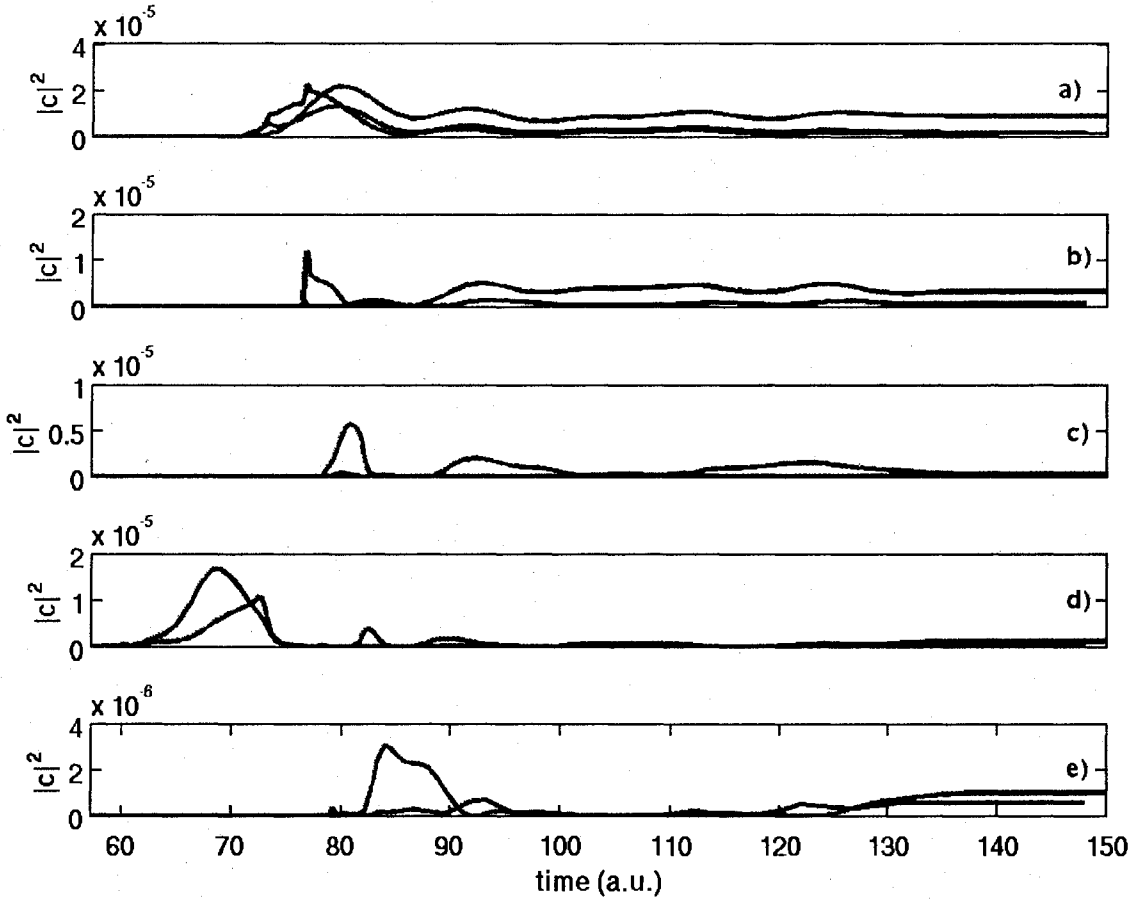

Figure 5.9. Plots of the populations in various states. a) the populations in the sixth state for the SGR, $|(\phi_6^{sgr}|\phi_6^{sgr})|$, (red) and for the level equations, $\left|(\phi_6^{le}|\phi_6^{le})\right|$, with 15 eigenfunctions (blue) and 7 eigenfunctions (green) b) the populations in the eighth state for the SGR, $|(\phi_8^{sgr}|\phi_8^{sgr})|$, (red) and for the level equations, $\left|(\phi_8^{le}|\phi_8^{le})\right|$, with 15 eigenfunctions (blue) c) the populations in the ninth excited state for the SGR, $|(\phi_9^{sgr}|\phi_9^{sgr})|$, (red) and for the level equations, $\left|(\phi_9^{le}|\phi_9^{le})\right|$, with 15 eigenfunctions (blue) d) the populations in the eleventh excited state for the SGR, $|(\phi_1 1^{sgr}|\phi_1 1^{sgr})|$, (red) and for the level equations, $\left|(\phi_1 1^{le}|\phi_1^{le})\right|$, with 15 eigenfunctions (blue) e) the populations in the thirteenth excited state for the SGR, $|(\phi_1 3^{sgr}|\phi_1 3^{sgr})|$, (red) and for the level equations, $\left|(\phi_1 3^{le}|\phi_1 3^{le})\right|$, with 15 eigenfunctions (blue)

Chapter 6

Conclusions

We have developed the complex scaling method and calculated the time independent eigenstates for both a one dimensional test model using UCS and for N_2^+ in two dimensions using SMECS. We implemented complex scaling by using a space grid and using a basis set in one dimension and then calculated the eigenstates. When we did we this for a system with an applied electric field and calculated the eigenstates we saw incredible agreement between the two. We were also able to bring our complex scaled eigenstates back into real space to allow proper calculations of the norm through the method of complex scaling. This is method is the first to be developed of it's kind and significantly broadens the number and types of problems that complex scaling can address.

We then went on to develop a set of coupled level equations which rely on the field dependent eigenstates for propagating our wavefunction in time as well as a method for directly propagating the wavefunction using the Hamiltonian. When we moved to time dependent simulations we have shown that the use of the "c-norm" fails when we apply a time dependent electric field but by using complex backscaling and enforcing the real space norm on our eigenfunctions we properly predict the resulting ionization. Furthermore, using the time independent energies we were able to explain the oscillations that we see in the ionization due to the ionization rates of the resonances. All of these results were compared to calculations done without complex scaling and excellent agreement was obtained. The final step to making complex backscaling a robust and practical tool is the issue of the orthogonality of the backscaled wavefunctions. When we backscale we lose the ability to track our wavefunction in terms of meaningful states and until this issue is resolved we will only be able to observe the norm of our wavefunction for meaningful results.

When we moved to two dimensions where we have yet to implement backscaling, we see that our time dependent calculations deviate, but we believe that implementing backscaling will alleviate such problems. With further development, the complex backscaling method could become a workhorse for calculating non-linear effects in a large variety of systems. Future work using the complex backscaling method will hopefully shed some light on problems such as non-sequential ionization and other intense field physics processes.

Appendix A

Calculating Eigenstates

To calculate the eigenvectors of a field free system, we start with a general Hamiltonian (written in atomic units).

$$\hat{H} = -\frac{1}{2}\nabla^2 + V(\vec{r}) \tag{A.1}$$

Where $V(\vec{r})$ is the electron nucleus potential and ∇^2 is the Laplacian. This can be written in 1D as

$$\hat{H} = -\frac{1}{2}\frac{d^2}{dx^2} + V(x) \tag{A.2}$$

The eigenfunctions and eigen-energies are then calculated by solving the time independent Schrödinger equation.

$$\hat{H}\psi = E\psi \tag{A.3}$$

A.1 Calculating Eigenfunctions on a space Grid

When setting up our Hamiltonian in the space grid representation (SGR), we assume a basis that is made up of step functions, so that there is one step function that corresponds to each point in our grid. When we calculate the Hamiltonian on this grid, except for the Laplacian, all of the terms are contained along the diagonal. If we have n_x points in our 1D simulation range, our Hamiltonian will be an $n_x \times n_x$ matrix. We can derive the Laplacian, at a point x_i, by using a Taylor series. If we have a function $f(x)$ and our grid has a step size of h, we can expand $f(x)$ about h, $-h$, $2h$, and $-2h$ to give

$$f(x_i + h) = f(x_i) + f'(x_i)\,h + \frac{f''(x_i)}{2}h^2 + \frac{f'''(x_i)}{6}h^3 + \frac{f''''(x_i)}{24}h^4 + O\left(h^5\right) \tag{A.4}$$

$$f(x_i - h) = f(x_i) - f'(x_i)\,h + \frac{f''(x_i)}{2}h^2 - \frac{f'''(x_i)}{6}h^3 + \frac{f''''(x_i)}{24}h^4 + O\left(h^5\right) \tag{A.5}$$

$$f(x_i + 2h) = f(x_i) + f'(x_i)\,2h + f''(x_i)\,2h^2 + \frac{4f'''(x_i)}{3}h^3 + \frac{2f''''(x_i)}{3}h^4 + O\left(h^5\right) \tag{A.6}$$

$$f(x_i - 2h) = f(x_i) - f'(x_i)\,2h + f''(x_i)\,2h^2 - \frac{4f'''(x_i)}{3}h^3 + \frac{2f''''(x_i)}{3}h^4 + O\left(h^5\right) \tag{A.7}$$

Adding equations A.4 and A.5 as well as A.6 and A.7 and ignoring terms of order h^5 gives,

$$f(x_i+h)+f(x_i-h)=2f(x_i)+f''(x_i)h^2+\frac{f''''(x_i)}{12}h^4 \tag{A.8}$$

$$f(x_i+2h)+f(x_i-2h)=2f(x_i)+f''(x_i)4h^2+\frac{4f''''(x_i)}{3}h^4 \tag{A.9}$$

$$\tag{A.10}$$

Then, getting rid of terms to order h^4 leaves us with

$$f''(x_i)=\frac{-f(x_i-2h)+16f(x_i-h)-30f(x_i)+16f(x_i+h)-f(x_i+2h)}{12h^2} \tag{A.11}$$

This means that by sampling from the left and the right of the point in question we can approximate the derivative using A.11.

Setting up our Hamiltonian, and applying a zero boundary condition gives us our symmetric block diagonal Hamiltonian of

$$\hat{H}=\begin{pmatrix} \frac{30}{24h^2}+V(x_1) & \frac{-16}{24h^2} & \frac{1}{24h^2} & 0 & 0 & \cdots \\ \frac{-16}{24h^2} & \frac{30}{24h^2}+V(x_2) & \frac{-16}{24h^2} & \frac{1}{24h^2} & 0 & \cdots \\ \frac{1}{24h^2} & \frac{-16}{24h^2} & \frac{30}{24h^2}+V(x_3) & \frac{-16}{24h^2} & \frac{1}{24h^2} & \cdots \\ 0 & \frac{1}{24h^2} & \frac{-16}{24h^2} & \frac{30}{24h^2}+V(x_4) & \frac{-16}{24h^2} & \cdots \\ 0 & 0 & \frac{1}{24h^2} & \frac{-16}{24h^2} & \frac{30}{24h^2}+V(x_5) & \cdots \\ \vdots & \vdots & \vdots & \vdots & \vdots & \ddots \end{pmatrix} \tag{A.12}$$

If we wish to add a time independent electric field, F, then all that is required is to add to each element H_{ii} an extra $-Fx_i$. Once we have obtained our Hamiltonian, we can calculate the eigenfunctions using a packaged eigensolver such as LAPACK or ARPACK. We decided to use Matlab to find the eigenfunctions, which implements LAPACK, for technical reasons explained in Chapter 4. With this method when the eigenfunctions are returned from the eigensolver, the eigenfunctions will be vectors that contain the value of the eigenfunction at each point in space (which is not the case when you use a basis).

If we are in 2D with n_x points in the x direction and n_y points in the y direction, then our plane of points must be represented as a vector, $\vec{v}$. ie

$$\vec{v}=\begin{pmatrix} x_1y_1 \\ x_1y_2 \\ x_1y_3 \\ \vdots \\ x_1y_{n_y} \\ x_2y_1 \\ x_2y_2 \\ x_2y_3 \\ \vdots \end{pmatrix} \tag{A.13}$$

and our Hamiltonian will be of size $n_xn_y \times n_xn_y$. Calculating the Hamiltonian in 2D is very similar to calculating the Hamiltonian in 1D. The Laplacian still has the terms which are ± 1

and ± 2 off the diagonal as in A.12, but now we have terms that are $\pm n_y$ and $\pm 2n_y$ in the same manner. Our diagonal term just gains an $30/24h_y^2$ where h_y is the y step size in y.

Implementing complex scaling for our Hamiltonian requires only a bit more work. From Eq. 2.12, the only terms not along the diagonal are again the Laplacian terms, which act like they have been transformed. This means that we must calculate the Laplacian as in Eq. A.12, but before we add the potential term, we must multiply both sides of our Laplacian matrix by the diagonal matrix $1/q(x)$. We can then add the diagonal terms of Eq. 2.12. In 2D, we need to calculate the second derivative for both x and y as two different matrices, and then multiply both sides of $\partial^2/\partial x^2$ by $1/q(x)$, and both sides of $\partial^2/\partial y^2$ by $1/p(y)$. Then they can be added together along with the diagonals to get the complex scaled matrix.

A.2 Calculating Eigenfunctions Using a Global Basis

As an alternative to the SGR method we can calculate the Hamiltonian by using our own basis and then calculating each of the matrix elements. This method makes for much smaller matrices to be diagonalized and allows us to know our basis analytically, but requires the basis to be tailored to the particular problem at hand as using an infinite basis set is impossible. For our calculations, we need an analytical basis that exists on the range $[-\infty\ \infty]$, and preferably is orthonormal. A basis that satisfies those properties, and allows us some freedom to customize the basis to our problems, are the scaled Hermite Gaussian functions. These are defined such that

$$\begin{aligned}
\zeta_0 &= \left(\frac{1}{w\sqrt{\pi}}\right)^{1/2} e^{-\frac{x^2}{2w^2}} \\
\zeta_1 &= 2\frac{x}{w}\left(\frac{1}{w\sqrt{\pi}}\right)^{1/2} e^{-\frac{x^2}{2w^2}} \\
&\vdots \\
\zeta_{n+1}(x) &= \frac{2x}{w}\zeta_n(x) - 2n\zeta_{n-1}(x)
\end{aligned} \tag{A.14}$$

Where w is a parameter controlling the width of the basis functions. The nth order Hermite Gaussian function is related to the nth order Hermite polynomial $H_n(x)$ by

$$\zeta_n = \left(\frac{1}{n!2^n w\sqrt{\pi}}\right)^{1/2} e^{-\frac{x^2}{2w^2}} H_n\left(\frac{x}{w}\right) \tag{A.15}$$

We can also relate the derivative of each Hermite Gaussian via

$$\zeta_n' = -\left(\frac{x}{w}\right)\zeta_n + \frac{\sqrt{2n}}{w}\zeta_{n-1} \tag{A.16}$$

Calculating the matrix elements of the Hamiltonian, H_{ij} is then just a matter of calculating

$$\begin{aligned} H_{ij} &= [\zeta_i|\,\hat{H}\,|\zeta_j] \\ &= \left[\zeta_i\left|-\frac{1}{2}\frac{d^2}{dx^2}+V(x)\right|\zeta_j\right] \\ &= \left[\zeta_i\left|-\frac{1}{2}\frac{d^2}{dx^2}\right|\zeta_j\right]+[\zeta_i\,|V(x)|\,\zeta_j] \end{aligned} \tag{A.17}$$

where our inner product, $[\zeta_i|\,\hat{O}\,|\zeta_j]$, is the traditional Hermitian norm, $\langle\zeta_i|\,\hat{O}\,|\zeta_j\rangle$, which we always use in when our operator is Hermitian

$$\langle\zeta_i|\,\hat{O}\,|\zeta_j\rangle = \int_{-\infty}^{\infty}\zeta_i^*\hat{O}\zeta_j dx. \tag{A.18}$$

When our operator is not Hermitian (which we shall assume for all subsequent derivations unless specified), which is the case for all complex scaled Hamiltonians then the norm, $[\zeta_i|\,\hat{O}\,|\zeta_j]$, which we use is the "c-norm", $(\zeta_i|\,\hat{O}\,|\zeta_j)$, as described in chapter 2.3

$$(\zeta_i|\,\hat{O}\,|\zeta_j) = \int_{-\infty}^{\infty}\zeta_i\hat{O}\zeta_j dx \tag{A.19}$$

Then to calculate the Laplacian term (assuming we are in a complex scaled space and use the "c-norm"), we may use integration by parts, and the fact that the basis functions vanish at $\pm\infty$

$$\begin{aligned} \left(\zeta_i\left|-\frac{1}{2}\frac{d^2}{dx^2}\right|\zeta_j\right) &= -\frac{1}{2}\int_{-\infty}^{\infty}\zeta_i\frac{d^2}{dx^2}\zeta_j dx \\ &= -\frac{1}{2}\int_{-\infty}^{\infty}\zeta_i\frac{d}{dx}\frac{d\zeta_j}{dx}dx \\ &= -\frac{1}{2}\,\zeta_i\frac{d\zeta_j}{dx}\Big|_{-\infty}^{\infty}+\int_{-\infty}^{\infty}\frac{d\zeta_i}{dx}\frac{d\zeta_j}{dx}dx \\ &= -\frac{1}{2}\int_{-\infty}^{\infty}\frac{d\zeta_i}{dx}\frac{d\zeta_j}{dx}dx \end{aligned} \tag{A.20}$$

Then diagonalizing this Hamiltonian gives eigenvalues which are the energies corresponding to an eigenvector of coefficients. When we wish to use the eigenfunctions in the basis method, given the basis functions ζ_i, the jth eigenfunction is obtained by a vector of coefficients from which you rebuild your eigenfunction. ie

$$\phi_j = \sum_i c_{ji}\zeta_i \tag{A.21}$$

One difficulty that was discovered when using a set of Hermite Gaussian functions with width w_1, was that if our eigenfunction had a finite value in a region extended from the center of our potential, then we must use many orders of Hermite Gaussian basis functions to capture the full eigenfunction. However, sometimes the increase in the number of Hermite Gaussian functions becomes quite substantial in order to reach out that far and the higher order Hermite Gaussians require a much smaller spatial step in order to resolve the faster oscillations. A solution to this is instead of using a single set of Hermite Gaussians to implement a second set with width w_2

where $w_2 > w_1$. This allows us to cover a larger range in space, while not having to deal with the fast oscillations which come with a single set of Hermite Gaussians. The downfall of this method, however, is that the basis set we are using stops being orthogonal and diagonalizing the Hamiltonian becomes a generalized eigenvalue problem.

This can be seen immediately if we write the action of the Hamiltonian on an eigenfunction.

$$\begin{aligned} \hat{H}\,|\phi) &= E\,|\phi) \\ &= E\sum_i c_i\,|\zeta_i) \end{aligned} \tag{A.22}$$

Then, if we project on it with $(\zeta_j|$ we obtain

$$\begin{aligned} (\zeta_j|\,\hat{H}\,|\phi) - E\,(\zeta_j|\phi) &= 0 \\ \sum_i c_i\,(\zeta_j|\,\hat{H}\,|\zeta_i) - E\sum_i c_i\,(\zeta_j|\zeta_i) &= 0 \end{aligned} \tag{A.23}$$

This is our regular eigenvalue equation when $(\zeta_j|\zeta_i) = \delta_{ij}$ giving

$$\begin{aligned} \sum_i c_i\,\langle\zeta_j|\,\hat{H}\,|\zeta_i\rangle - E\sum_i c_i &= 0 \\ (\mathbf{H} - \lambda\mathbf{I})\,\phi &= 0 \end{aligned} \tag{A.24}$$

when $(\zeta_j|\zeta_i) \neq \delta_{ij}$, then we have a generalized eigenvalue problem

$$(\mathbf{H} - \lambda\mathbf{O})\,\phi = 0 \tag{A.25}$$

where the matrix elements of our orthogonality matrix, $\mathbf{O}$, are given by

$$O_{ji} = (\zeta_j|\zeta_i) \tag{A.26}$$

We can rewrite Eq. A.25 as long as our basis functions are linearly independent, which means our orthogonality matrix is invertable

$$\left(\mathbf{O^{-1}H} - \lambda\mathbf{I}\right)\phi = 0 \tag{A.27}$$

A.2.1 Calculating the Orthogonality Matrix

Calculating the orthogonality matrix is not as trivial as it may seem. Due to the fast oscillations of the Hermite Gaussians using simple integration schemes is impossible. For instance, if we have our basis functions ζ_i, and we have our grid at the points x_1, x_2, ...x_n and evenly spaced by dx we could normally approximate the integral by the trapezoidal rule. But, using such an integral would mean that if we have a Hermite Gaussian up to order m, then the orthogonality matrix has the possibility of having m^2 roots, so for $m = 50$ we would need approximately 2500 points just to resolve all of the zeros of that function let alone resolve the function well enough to integrate it in that region. This is further complicated when we perform the backscaling described in Section

2.4, as the backscaled states don't fall off exponentially, but quickly diverge. The best way to perform such integrations is to use the Gaussian quadrature method of integration described in Appendix B.

The orthogonality matrix is required for more than just calculating the generalized eigenvalue problem. When we wish to calculate the norm of the complex scaled wavefunction, we also must take into account the orthogonality. For instance, when we have our eigenfunction $\phi_m = \sum c_{mi}\zeta_i$, we can calculate the norm of the eigenfunction by

$$\begin{aligned} N_m &= (\phi_m|\phi_m) \\ &= \left(\sum_i c_{mi}\,(\zeta_i|\right)\left(\sum_j c_{mj}\,|\zeta_j)\right) \\ &= \sum_{ij} c_{mi}c_{mj}\,(\zeta_i|\zeta_j) \\ &= \sum_{ij} c_{mi}c_{mj}O_{ij} \end{aligned} \tag{A.28}$$

also if we wish to find out the probability of our wavefunction $\psi = \sum_n a_n\phi_n$ being in the eigenstate ϕ_m, it is related to the orthogonality matrix by

$$\begin{aligned} (\phi_m|\psi) &= \sum_n a_n\,(\phi_m|\phi_n) \\ &= \sum_n a_n\left(\sum_i c_{mi}\,(\zeta_i|\right)\left(\sum_j c_{nj}\,|\zeta_j)\right) \\ &= \sum_{nij} a_n c_{mi}c_{nj}\,(\zeta_i|\zeta_j) \end{aligned} \tag{A.29}$$

Thus, if we wish to calculate these quantities we must have the orthogonality matrix calculated very precisely and the best method for doing this is using Gaussian Quadrature.

Appendix B

Gaussian Quadrature

When doing numerical integration of a function $f(x)$, you may approximate the integral by selecting a range of points $\{x_i\}$ spaced by a distance Δx, and sum the value of the function at these points, where you will obtain numerical convergence if Δx is chosen small enough. This method is easily implemented and is usually sufficient for functions which vary slowly within the range of integration. When we have functions which are not slowly oscillating, it can become very cumbersome and numerically intensive to calculate integrals unless a more exact method is used.

Gauss gave a proof that on the finite interval $[-1\ 1]$ that the best possible accuracy that can be obtain by selecting n points is when the n points correspond to the roots of the Legendre polynomial $P_n(x)$. For this case our integration becomes

$$\int_{-1}^{1} f(x)\,dx \simeq \sum_{i=1}^{n} \lambda_{i,n} f(x_{i,n}) \tag{B.1}$$

where $\{x_i\}$ are the roots of $P_n(x)$ and the numbers $\lambda_{i,n}$ are the Christoffel or Cotes numbers. B.1 is an exact formula whenever $f(x)$ is a polynomial of degree $2n-1$ or less.

If our range of integration is $[-\infty\ \infty]$ then we may use the same method except now we use the Hermite polynomials, $H_n(x)$, which are related to our Hermite Gaussian basis functions by A.15. We then sample points at the zeros of our nth order Hermite polynomial $\{x_i\}$, and we may approximate the integral using a weight function as

$$\int_{-\infty}^{\infty} f(x)\,e^{-x^2}\,dx \simeq \sum_{i=1}^{n} \lambda_{i,n} f(x_{i,n}) \tag{B.2}$$

and the set of Christoffel numbers is given by

$$\lambda_{i,n} = \frac{\sqrt{\pi}\,2^{n+1}n!}{\left[H_n'(x_{i,n})\right]^2} \tag{B.3}$$

Again we have, if $f(x)$ is a polynomial of degree $2n-1$ or less then this integration formula is exact. This allows us to normalize our inner products much more accurately, for example normalizing the mth Hermite Gaussian (with $w=1$) gives

$$\begin{aligned}\int_{-\infty}^{\infty} \left[\zeta_m(x)\right]^2 dx &= \int_{-\infty}^{\infty} \left[H_m(x)\right]^2 e^{-x^2} dx \\ &\simeq \sum_{i=1}^{n} \lambda_{i,n} \left[H_m(x_{i,n})\right]^2\end{aligned} \tag{B.4}$$

Where $m < n$ in order to be exact and if $m = n$ we will get zero as we only sample at the zeros of H_n.

References

[1] T. Brabec M. Y. Ivanov and P. B. Corkum. Coulomg focusing in intense field atomic processes. *Phys. Rev. A.*, 54:2551, 1995.

[2] D. Zeidler A. Staudte A. B. Bardon D. M. Villeneuve R. Dörner and P. B. Corkum. Controlling attosecond double ionization dynamics via molecular alignment. *Phys. Rev. Lett.*, 95:203003, 2005.

[3] C. McDonald. Master's thesis. 2007.

[4] S. Baker J.S. Robinson C.A. Haworth H. Teng R.A. Smith C.C. Chirilă M. Lein J.W.G. Tisch and J.P. Marangos. Probing proton dynamics in molecules on an attosecond time scale. *Science*, 312:424, 2006.

[5] M. Foster and J. Colgan. Charge-dependent effects in double photoionization of he-like ions. *J. Phys. B*, 39:5067, 2006.

[6] M. Uiberacker Th. Uphues M. Schultze A. J. Verhoef V. Yakovlev M. F. Kling J. Rauschenberger N. M. Kabachnik H. Schrder M. Lezius K. L. Kompa H.-G. Muller M. J. J. Vrakking S. Hendel U. Kleineberg U. Heinzmann M. Drescher and F. Krausz. Attosecond real-time observation of electron tunnelling in atoms. *Nature*, 446:627, 2007.

[7] L.S. Cederbaum G. A. Worth. Beyond born oppenheimer: Molecular dynamics through a conical intersection. *Annu. Rev. Phys. Chem.*, 55:127, 2004.

[8] N. Moiseyev. Quantum theory of resonances: calculating energies, widths and cross-sections by complex scaling. *Phys. Rept.*, 302:211, 1998.

[9] A. J. F. Siegert. On the derivation of the dispersion formula for nuclear reactions. *Phys. Rev.*, 56:750, 1939.

[10] W. P. Reinhardt. Complex coordinates in the theory of atomic and molecular structure and dynamics. *Ann. Rev. Phys. Chem.*, 33:223, 1982.

[11] D. Byrum T. N. Rescigno, M. Baertschy and C. W. McCurdy. Making complex scaling work for long-range potentials. *Phys. Rev. A*, 55:4253, 1997.

[12] B. Simon. Resonances in n-body quantum systems with dilatation analytic potentials and the foundations of time-dependent perturbation theory. *Ann. Math.*, 97:247, 1973.

[13] Hans O. Karlsson. Accurate resonances and effective absorption of flux using smooth exterior scaling. *J. Chem. Phys.*, 109:9366, 1998.

[14] B. Simon. The definition of molecular resonance curves by the method of exterior complex scaling. *Phys. Lett. A*, 71:211, 1979.

[15] Avner Fleischer Ido Gilary and Nimrod Moiseyev. Calculations of time-dependent observables in non-hermitian quantum mechanics: The problem and a possible solution. *Phys. Rev. A*, 72:012117, 2005.

[16] M Plummer and J F McCann. Field-ionization rates of the hydrogen molecular ion. *J. Phys. B*, 29:4625, 1996.

[17] M Plummer and J F McCann. Complex-basis-function floquet calculations of multiphoton ionization rates in hydrogen systems. *J. Phys. B*, 28:4073, 1995.